

**This item is the archived peer-reviewed author-version of:**

The effect of oxygen availability on long-distance electron transport in marine sediments

**Reference:**

Burdorf Laurine D. W., Malkin Sairah Y., Bjerg Jesper T., van Rijswijk Pieter, Criens Francis, Tramper Anton, Meysman Filip.- The effect of oxygen availability on long-distance electron transport in marine sediments  
Limnology and oceanography - ISSN 0024-3590 - 63:4(2018), p. 1799-1816  
Full text (Publisher's DOI): <https://doi.org/10.1002/LNO.10809>  
To cite this reference: <https://hdl.handle.net/10067/1531680151162165141>

1 *This is the pre-peer reviewed version, which has been published in final form at*  
2 *<https://doi.org/10.1002/lno.10809>. This article may be used for non-commercial purposes in*  
3 *accordance with Wiley Terms and Conditions for Use of Self-Archived Versions.*

# 4

# 5

# 6 **The effect of oxygen availability on**

# 7 **long-distance electron transport in marine**

# 8 **sediments**

9

10 Laurine D.W. Burdorf <sup>1,2\*</sup>

11 Sairah Y. Malkin <sup>2,#</sup>

12 Jesper Tataru Bjerg <sup>3</sup>

13 Pieter van Rijswijk <sup>1</sup>

14 Francis Criens <sup>1</sup>

15 Anton Tramper <sup>1</sup>

16 Filip J. R. Meysman <sup>1,2</sup>

17

18 <sup>1</sup> Department of Estuarine and Delta Systems, NIOZ Royal Netherlands Institute for Sea  
19 Research and Utrecht University, Korringaweg 7, 4401 NT Yerseke, the Netherlands

20 <sup>2</sup> Department of Analytical, Environmental and Geo-Chemistry, Vrije Universiteit Brussel,  
21 Pleinlaan 2, 1050 Brussel, Belgium

22 <sup>3</sup> Department of Bioscience, Microbiology Section, Aarhus University, Ny Munkegade 116,  
23 8000 Aarhus, Denmark

24 # current address: Horn Point Laboratory, University of Maryland Center for Environmental  
25 Science (UMCES), Cambridge, MD, USA

26

27 \* Corresponding author: [laurine.burdorf@gmail.com](mailto:laurine.burdorf@gmail.com)

29 **ABSTRACT**

30 Cable bacteria are long, multicellular, filamentous bacteria that can conduct electrons over  
31 centimeter distances in marine and freshwater sediments. Recent studies indicate that cable  
32 bacteria are widely present in many coastal environments, where they exert a major influence  
33 on the biogeochemistry of the sediment. Their energy metabolism is based on the aerobic  
34 oxidation of sulfide, and hence to better understand their natural occurrence and distribution,  
35 we examined the growth and activity of cable bacteria in relation to bottom water  
36 oxygenation. To this end, we conducted laboratory sediment incubations at four different O<sub>2</sub>  
37 levels in the overlying water (10, 20, 40, and 100 % air saturation). The abundance of cable  
38 bacteria was determined by fluorescence in situ hybridisation, while their activity was  
39 quantified via microsensor profiling and geochemical pore water analysis. Cable bacteria did  
40 not develop in the 10% O<sub>2</sub> incubation, but were present and active in all higher O<sub>2</sub> levels.  
41 These data show that microbial long-distance electron transport is not limited to fully oxic  
42 environment, but can occur under a wide range of bottom water oxygen concentrations.  
43 However, the growth rate was notably slower at lower oxygen concentrations, suggesting a  
44 reduced metabolic activity of the population when the O<sub>2</sub> supply becomes restricted. Finally,  
45 in response to lower O<sub>2</sub> levels, cable bacteria filaments appear to partially crawl out of the  
46 sediment and extend into the overlying water, likely to enhance their oxygen supply.

47

## 48 **Introduction**

49 In 2010, close inspection of the geochemistry of marine sediments unveiled the existence of  
50 electrical currents in the top centimeters (Nielsen et al. 2010). Subsequently, it was discovered  
51 that these electrical currents were mediated by “cable bacteria”, which take advantage of  
52 long-distance electron transport (LDET) for their sulfur oxidizing metabolism (Pfeffer et al.  
53 2012). Similar to trees on land, which have evolved transport vessels to connect two spatially  
54 separated metabolic resources (i.e. nutrients and water from the ground and light from the  
55 sky), cable bacteria bridge the distance between two key resources for their energy  
56 metabolism (i.e. oxygen and sulfide) by means of electron transport. The bottom cells of the  
57 cable filament receive electrons from the oxidation of sulfide, which is abundant in the deeper  
58 anoxic zone of the sediment, being the end product from sulfate reduction, which can be  
59 responsible for 50 - 90% of the total carbon mineralization in coastal sediments (Jørgensen  
60 1982; Kristensen et al. 2008). The electrons derived from sulfide oxidation are transported  
61 from cell to cell to the oxic zone, where they are used in the reduction of oxygen (the overall  
62 process is called electrogenic sulfur oxidation or e-SO<sub>x</sub>). The flow of electrons through the  
63 cable bacteria is accompanied by a counter-directional flow of cations through the sediment  
64 pore water (Risgaard-Petersen et al. 2015), and so the sediment is effectively transformed into  
65 a biogeobattery with an anode (sulfide oxidation reaction) and a cathode (oxygen reduction  
66 reaction).

67       Electrogenic sulfur oxidation has recently been found in a wide variety of habitats in  
68 marine and freshwater environments across the globe (Malkin et al. 2014; Risgaard-Petersen  
69 et al. 2015; Burdorf et al. 2017). Productive coastal sites, characterized by high organic matter  
70 loading and a (periodic) absence of bioturbation seem to be a particularly suitable habitat for  
71 cable bacteria. More specifically, e-SO<sub>x</sub> activity has been demonstrated to occur in intertidal  
72 flats (Malkin et al. 2014), bivalve reefs (Malkin et al. 2017; Burdorf et al. 2017), mangrove

73 sediments (Burdorf et al. 2016), seasonally oxygen depleted marine basins (Sayama 2011;  
74 Malkin et al. 2014; Seitaj et al. 2015), salt marshes (Malkin et al. 2014) and fjord sediments  
75 (Burdorf et al. 2017). The distribution of LDET in freshwater sediments is less well  
76 characterized, but Risgaard-Petersen et al. (2015) demonstrated the process in a small river,  
77 and Müller et al. (2016) reported the presence of cable bacteria in a polluted aquifer.

78         Given the widespread distribution of long-distance electron transport in marine  
79 sediments (Burdorf et al. 2017), and its large effect on the sediment geochemistry (Risgaard-  
80 Petersen et al. 2012; Meysman et al. 2015), it is important to unravel the environmental  
81 controls that constrain its distribution within in the seafloor. At present however, the  
82 metabolism, ecological niche and basic life history traits of the cable bacteria that perform  
83 LDET are not well characterized. Foremost, a suitable supply of the electron donor (sulfide)  
84 and the electron acceptor (oxygen or nitrate) appear to be key requirements (Nielsen et al.  
85 2010; Marzocchi et al. 2014; Malkin et al. 2014; Meysman et al. 2015). Furthermore, Malkin  
86 et al. (2014) speculated that an additional environmental control on the natural distribution of  
87 cable bacteria could be the presence of bioturbating fauna. However, the mechanism  
88 underlying this control is not yet clear, and cable bacteria have been reported to occur in  
89 bioturbated sediments (Burdorf et al., 2017).

90         To better understand the distribution of LDET in the present ocean as well as on  
91 geological timescales, this study examines the influence of the oxygen on the population  
92 growth of cable bacteria. To this end, the development of cable bacteria was tracked in long-  
93 term sediment incubations in which the overlying water was poised at different oxygen levels.  
94 We enumerated the density of cable bacteria by a molecular staining and microscopy, and  
95 quantified the metabolic activity through microsensor profiling and geochemical pore water  
96 analysis.

97 **Material and Methods**

98 **Sediment collection and preparation**

99 Sediment was collected in February 2013 in Lake Grevelingen, a seasonally hypoxic saline  
100 water body in the Rhine-Meuse-Scheldt delta in the south-west of The Netherlands. Previous  
101 studies have shown that cable bacteria are yearly recurrent within the surface sediments of  
102 Lake Grevelingen (Seitaj et al. 2015; Burdorf et al. 2017) reaching high densities in winter  
103 and spring within the deeper parts of the lake (> 15 m water depth) (Seitaj et al. 2015).

104 Sediment was retrieved using a single core gravity corer (UWITEC, Austria) at the  
105 Den Osse S1 site (51° 44' 46.3" N 3° 52' 45.1" E, water depth 23 m). The top layer of  
106 sediment (~ 10 cm) was sliced off from sediment cores, and transferred into two plastic  
107 containers (volume: 28 L), which were filled to the rim and capped with gas-tight lids. The  
108 sediment was subsequently stored at 6 °C for 13 days. The sediment was cohesive and fine-  
109 grained (medium grain size: 16 µm; porosity 0.88), and rich in organic matter (organic carbon  
110 content: 3.0% of dry weight sediment) and carbonate minerals (CaCO<sub>3</sub> content: 22% of dry  
111 weight sediment). Sediment properties are summarized in Table 1.

112 Right before the start of the experiment, the sediment was prepared for incubation as  
113 described in Burdorf et al. (2017). First, the sediment was sieved over a 1 mm mesh to  
114 remove fauna and small debris (i.e. shells or rocks that could damage the electrodes during  
115 microsensor profiling). After sieving, the sediment was homogenized and packed into plastic  
116 core liners (inner diameter: 12.5 cm, core liner height: 10 cm, sediment height: 10 cm).  
117 Homogenization ensured that starting conditions were similar in all incubated sediment cores.  
118 Sediment cores were finally transferred to a custom-built incubation set-up (as described  
119 below).

120 **Sediment incubations**

121 Sediment cores were incubated at four different oxygen levels (resp. 10, 20, 40, 100% O<sub>2</sub> air  
122 saturation, corresponding to 25, 51, 102, and 255 μmol L<sup>-1</sup> O<sub>2</sub> at a salinity of 28 and  
123 temperature of 18 °C). Sediment incubations lasted over a period of three months (109 days).  
124 For each O<sub>2</sub> treatment, a separate incubation set-up was constructed, which was composed of  
125 two cylindrical incubation chambers through which seawater recirculated in a closed-circuit  
126 (Fig.1). The first chamber functioned as the sediment incubation chamber (diameter: 28 cm,  
127 total volume ~15 L) and held two replicate sediment cores submerged under water. The  
128 second chamber (diameter: 13.2 cm, volume ~4 L) functioned as the water reservoir (Fig.1).  
129 Recirculation of seawater was driven by a water pump (Eheim, 1250 universal pump,  
130 Germany), which was positioned in the water reservoir. Water was pumped from the water  
131 reservoir via gas-tight tubing to the sediment incubation chamber (inlet located at about ¾ of  
132 the chamber height), and returned to the water reservoir through a connection in the top of the  
133 sediment incubation chamber. In the water reservoir, the oxygen level was continuously  
134 monitored with an oxygen sensor (Hamilton VisiFerm DO Arc 120 optode, USA) in order to  
135 maintain the oxygen concentration of the recirculating water at a stable, predefined level.  
136 When the oxygen level dropped below 2.5% of the desired O<sub>2</sub> concentration, a switch opened  
137 the gas connection of an air-pump (Easy-load L/S, Masterflex, USA). Similarly, when oxygen  
138 levels exceeded 2.5% over the desired O<sub>2</sub> concentration, the connection to a gas bottle (N<sub>2</sub>  
139 with 400 ppm CO<sub>2</sub>) was opened, bubbling the water reservoir until oxygen levels dropped  
140 again within the desired range. The four incubation set-ups (one for each O<sub>2</sub> treatment) were  
141 installed in a climate-regulated room, which was held at 18°C. To minimize the availability of  
142 nitrate as an alternative electron-acceptor in electrogenic sulphur oxidation (Marzocchi et al.,  
143 2014), low nutrient sea water (NO<sub>3</sub> concentration < 0.1 μmol L<sup>-1</sup>) was used as the  
144 recirculating water in all set-ups.

145 **Microsensor depth profiling**

146 The metabolic activity of cable bacteria was assessed via high-resolution depth profiles of pH,  
147 H<sub>2</sub>S and O<sub>2</sub> (Nielsen et al. 2010; Meysman et al. 2015). Depth profiles were recorded using  
148 commercial amperometric and potentiometric micro-electrodes and a motorized  
149 micromanipulator (Unisense A.S. Denmark, tip sizes pH: 200 μm, H<sub>2</sub>S 100 μm, O<sub>2</sub>: 50 μm).  
150 Sensors were calibrated by standard calibration procedures as described previously (Malkin et  
151 al. 2014: H<sub>2</sub>S: 3 to 5 point standard curve using Na<sub>2</sub>S standards; O<sub>2</sub>: 2 point calibration using  
152 100% in air bubbled seawater and the anoxic zone of the sediment; pH: 3 NBS standards and  
153 TRIS buffer). The pH data are reported on the total pH scale and  $\Sigma\text{H}_2\text{S} = [\text{H}_2\text{S}] + [\text{HS}^-]$  was  
154 calculated from H<sub>2</sub>S and pH values recorded at the same depth using the R package *AquaEnv*  
155 (Hofmann et al. 2010).

156         Microsensor profiling was done at seven consecutive time points during the  
157 experiment (2, 16, 25, 39, 52, 69 and 109 days after the start of the incubation). At each time  
158 point, two replicate profiles per sensor were recorded in each of the two replicate sediment  
159 cores in all four O<sub>2</sub> treatments. To enable microsensor profiling, the water circulation was  
160 temporarily stopped, and the lid of the incubation chamber was taken off. A custom-built  
161 sensor holder enabled to record the depth profiles of pH, H<sub>2</sub>S and O<sub>2</sub> simultaneously (to  
162 minimize profiling time and therefore the intrusion of oxygen in the incubation chamber).  
163 Although microsensor depth profiling always took less than 1.5 hours per treatment, it  
164 involved a small but unavoidable disturbance of the oxygen conditions in the set-ups (max.  
165 ~30% O<sub>2</sub> increase). Set-ups returned within 6 hours to their target oxygen levels after  
166 profiling was completed.

167         The microsensor data was used to calculate two proxies for the metabolic activity of  
168 cable bacteria following the procedure as detailed in Burdorf et al. (2016). A first proxy is the  
169 extent of the suboxic zone  $\Delta L$ , defined as the zone between the oxygen penetration depth

170 (OPD, depth at which  $[O_2] < 1 \mu\text{mol L}^{-1}$ ) and the sulfide appearance depth (SAD, depth at  
171 which  $[H_2S] > 1 \mu\text{mol L}^{-1}$ ). The suboxic zone reveals the depth horizon over which of cable  
172 bacteria actively remove both oxygen and sulfide by e-SOx (Meysman et al. 2015). As  
173 described in Schauer et al. (2014) the suboxic zone  $\Delta L$  also closely tracks the depth  
174 distribution of the filament density during the temporal development of a cable bacteria  
175 population. The second proxy of cable bacteria activity is the magnitude of the observed pH  
176 excursions in the pore water. The metabolic activity of cable bacteria typically generates large  
177 gradients in the pH of the pore water, and to this end, the quantity  $\Delta\text{pH}$  is defined as the  
178 difference between the maximum pH in the oxic zone and the minimum pH in the suboxic  
179 zone. We note that the amplitude of the observed pH excursions is dependent on the acid-base  
180 buffering capacity of sediment (e.g.  $\text{CaCO}_3$  precipitation and dissolution can modulate the  
181 observed pH excursions). Therefore, it is difficult to attribute  $\Delta\text{pH}$  to a single factor across  
182 different sediments. Yet, when using the same sediment (as is done here), the  $\Delta\text{pH}$  provides a  
183 good proxy to compare cable bacteria activity between different treatments and time points.

#### 184 **Pore water sampling**

185 The pore water geochemistry was examined in detail at one time point (39 days after the start  
186 of the incubation). Pore water was retrieved and analyzed for  $\text{Fe}^{2+}$ ,  $\text{Mn}^{2+}$ ,  $\text{Ca}^{2+}$ ,  $\text{NH}_4^+$ ,  $\text{SO}_4^{2-}$   
187 and  $A_T$  (total alkalinity). To this end, small plastic core-liners (inner diameter 36 mm) were  
188 pushed carefully into the center of each of the two sediment cores in all incubation setups  
189 (total: 8 subcores). These subcores were carefully expelled and immediately transferred to an  
190 anaerobic glove box (Coy Lab Products, USA;  $\text{N}_2$  atmosphere with 3-5%  $\text{H}_2$  and 390  $\mu\text{atm}$   
191  $\text{CO}_2$ ). Each subcore was sectioned at 0.5 cm intervals up to 4 cm and at 1 cm intervals up to  
192 10 cm, thus resulting in a maximum of 15 sediment slices per subcore. Each sediment slice  
193 was deposited into a 50 mL polypropylene centrifuge tube (TTP, Switzerland) closed off  
194 inside the glove box, and transferred to a centrifuge outside the glove box (Sigma 3-18KS,

195 Sigma Laborzentrifugen GmbH, Germany). After centrifugation (3000 rpm, 10 minutes), the  
196 centrifuge tubes were transferred back inside the glove box, and the supernatant was filtered  
197 through a 0.45 µm cellulose filter (Millex-HA Filter, Merck Millipore, USA) and distributed  
198 over the sample containers for the different analyses.

199         Subsamples (50 µL of filtered pore water) for cation analysis ( $\text{Ca}^{2+}$ ,  $\text{Fe}^{2+}$ ,  $\text{Mn}^{2+}$ ) were  
200 fixed immediately using 2 µL  $\text{HNO}_3$  (65%, suprapure, Merck, USA) in a 15 mL  
201 polypropylene centrifuge tube (TTP, Switzerland) and stored at 4°C until analysis. Prior to  
202 analysis, the samples were diluted 50 times using a mixture of artificial seawater (salinity:  
203 35), 2%  $\text{HNO}_3$  and an internal standard (Ytterbium at 0.2 mg L<sup>-1</sup>). Total concentrations of  
204 dissolved cations were subsequently determined using Inductively Coupled Plasma – Optical  
205 Emission Spectroscopy (ICAP 6600 ThermoFisher, USA).

206         Subsamples for  $\text{NH}_4^+$  analyses (200 µL of filtered pore water) were diluted 25 times  
207 with low nutrient seawater ( $[\text{NH}_4^+] < 1 \mu\text{M}$ ) in a 6 mL plastic vial (Pico Prias Vial, Perkin  
208 Elmer, USA) and stored at 4°C for < 48 hours before analysis. The samples were then  
209 analyzed using standard colorimetric analysis on a SEAL QuAAtro segmented flow analyzer  
210 (Aminot et al. 2009).

211         Subsamples for  $\text{SO}_4^{2-}$  analysis (250 µL of filtered pore water) were fixed with 1 mL of  
212 a 10 mM ZnAc solution in a 2 mL microcentrifuge tube and stored at -20 °C. The  $\text{SO}_4^{2-}$  was  
213 determined by ion chromatography using a  $\text{Na}_2\text{CO}_3$  (3.5 mM) and  $\text{NaHCO}_3$  (1.0 mM) buffer  
214 as eluent on a Dionex AS14 analytical column (Thermo Scientific) equipped with  
215 conductivity detection (ED40 electrochemical detector LC-02).

216         Subsamples (350 µL) for alkalinity ( $A_T$ ) analysis were collected in 350 µL glass vials  
217 and poisoned with 3.5 µL saturated  $\text{HgCl}_2$  solution. The  $A_T$  determination was based on the  
218 analysis of Dissolved Inorganic Carbon (DIC) after equilibration with an ambient atmosphere.  
219 To this end, the pore water was exposed for sufficiently long time in the  $\text{N}_2/\text{CO}_2$  glove box, so

220 that CO<sub>2</sub> and H<sub>2</sub>S could evade until equilibrium was reached. Subsequently, DIC was  
221 analyzed using a Segmented Flow Analyzer (San++ SKALAR) according to the method of  
222 Stoll et al. (2001). The carbonate equilibrium in seawater can be fully determined from two  
223 variables at steady-state (Dickson et al. 2007). In our case, the DIC was measured, while the  
224 pCO<sub>2</sub> in the atmosphere was known (pCO<sub>2</sub> = 390 μatm). Based on this information, we  
225 calculated the A<sub>T</sub> value at each depth using the standard acid-base relations implemented in  
226 the *AquaEnv* package (input parameters: temperature, salinity, DIC, pCO<sub>2</sub>, total NH<sub>4</sub><sup>+</sup>  
227 concentration as measured, total borate concentration as estimated from salinity) in the R  
228 package *AquaEnv* (Hofmann et al. 2010). In these calculations, we assume that all H<sub>2</sub>S has  
229 evaded, while we ignore the acid-base contributions of phosphate and silicate, which only  
230 contribute marginally to the alkalinity of the pore water.

231

### 232 **Flux calculations**

233 Diffusive oxygen uptake rate in the sediment was calculated from the oxygen depth profiles

234 using Fick's first law:  $J_{O_2} = \phi \frac{D_{O_2}}{1 - 2\ln(\phi)} \frac{d[O_2]}{dx}$ . Here, the diffusive oxygen flux ( $J_{O_2}$ ) is

235 calculated using the slope of the oxygen concentration depth profile ( $\frac{d[O_2]}{dx}$ ) and the

236 molecular diffusion coefficient ( $D_{O_2}$ ) corrected for tortuosity ( $1 - 2\ln(\phi)$ ) and the mean

237 porosity over the oxic zone ( $\phi = 0.88$ , Table 1). The molecular diffusion coefficient was

238 calculated in R using the *marelac* package (Soetaert et al. 2010a) taking into account the

239 temperature (18 °C) and salinity (28) of the incubations. Similarly the upward flux of ΣH<sub>2</sub>S

240 was calculated using the slope of the ΣH<sub>2</sub>S depth profile using Fick's first law at the base of

241 the suboxic zone using the diffusion coefficient for H<sub>2</sub>S. Finally upward and downward fluxes

242 were estimated from the iron pore water profiles using a similar approach and the molecular  
243 diffusion coefficient for ferrous iron ( $\text{Fe}^{2+}$ ).

244

#### 245 **Fluorescent in situ Hybridization (FISH)**

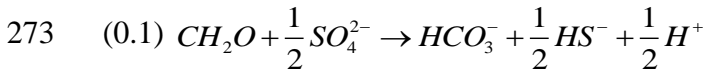
246 We used Fluorescent in situ Hybridization (FISH) to quantify the abundance of cable bacteria  
247 as a function of depth into the sediment. One sediment subcore was taken per oxygen  
248 treatment (total 4 cores) after 39 days of incubation and sliced at 0.5 cm intervals up to 5 cm  
249 deep (10 slices per core). Each sediment slice was homogenized and 0.5 mL of sediment was  
250 mixed with 0.5 mL 99% ethanol and preserved in  $-20^{\circ}\text{C}$ . We followed the FISH protocol  
251 described in Schauer et al. (2014) and the quantification procedure as specified in Seitaj et al.  
252 (2015). In short, subsamples of 100  $\mu\text{l}$  were transferred in 500  $\mu\text{l}$  of a 1:1 mixture of  
253 PBS/ethanol, and subsequently, 10  $\mu\text{l}$  of this mixture was filtered through a polycarbonate  
254 membrane filter (type GTTP, pore size 0.2  $\mu\text{m}$ , Millipore, USA). Hybridization of the FISH-  
255 probe (DSB706 at 35% formamide concentration) was performed according to previously  
256 published FISH protocols (Pernthaler et al. 2001, 2002). Samples were counterstained with  
257 DAPI and subsequently visualized with an epifluorescence microscope (Zeiss Axioplan,  
258 Germany) at 100x magnification. To quantify the cable bacteria, the filters were separated  
259 into discrete virtual fields-of-view. Each field-of-view, or field, is the area of the filter as seen  
260 through the microscope at 100x magnification (or 105 x 141  $\mu\text{m}$ ). In each field, the length of  
261 and diameter of all observed cable bacteria filaments are determined. In total 200 fields per  
262 sample were analyzed. In all treatments, cable bacteria abundances are reported as filament  
263 length per volumetric unit (i.e., meter of filament per  $\text{cm}^3$  of bulk sediment). Cable bacteria  
264 abundances were also integrated over depth and expressed per unit area of sediment surface  
265 (i.e., meter of filament per  $\text{cm}^2$  of sediment).

266

267 **Biogeochemical model analysis**

268 A simplified reactive transport model was constructed to estimate the mineralization rate of  
269 organic matter by fitting numerical model solutions to the estimated  $A_T$  and  $NH_4^+$   
270 concentration depth profiles. In this model, we assumed that sulfate reduction is the dominant  
271 pathway of organic matter mineralization.

272



274

275 Furthermore, we ignore the removal of ammonium through nitrification and anammox, and  
276 we ignore carbonate dissolution/precipitation and cable bacteria metabolism in the case of  $A_T$ .

277 If  $R_{min}$  is the mineralization rate of organic matter and  $\gamma_{CN}$  is the C/N ratio, the associated  
278 mass balance equations for  $A_T$  (eq. 1.2) and  $NH_4^+$  (eq. 1.3) become:

279 (0.2)  $\frac{\partial}{\partial x} \left[ \phi D_{A_T} \frac{\partial A_T}{\partial x} \right] + R_{min} = 0$

280 (0.3)  $\frac{\partial}{\partial x} \left[ \phi D_{NH_4^+} \frac{\partial [NH_4^+]}{\partial x} \right] + \frac{1}{\gamma_{CN}} R_{min} = 0$

281

282 The underlying assumptions are that the sediment is in steady-state, molecular diffusion is the  
283 only important transport process, the porosity  $\phi$  is constant with depth, and that  
284 mineralization rate  $R_{min}$  is also constant with depth. The diffusion coefficients ( $D_{A_T}$ ,  $D_{NH_4^+}$ )  
285 were calculated as a function of the temperature (18 °C) and salinity (28) of the sediment  
286 incubation using the R package *marelac* (Soetaert et al. 2010a), assuming the diffusion  
287 coefficient of bicarbonate is representative for  $A_T$ .

288 As boundary conditions, the model is constrained at the sediment-water interface by  
289 fixed concentrations in the overlying water ( $A_T$ : 4.2 mmol L<sup>-1</sup> and  $NH_4^+$ : 0.1 mmol L<sup>-1</sup>) and a  
290 no gradient condition at the lower boundary of the sediment domain (10 cm).

291 The numerical solution for the two partial differential equations (eq. 1.2 and 1.3) was  
292 implemented in R following the approach outlined in Soetaert and Meysman (2012). In short,  
293 the spatial derivatives of the partial differential equations were expanded as a finite difference  
294 grid (200 equidistant layers over the sediment domain of 10 cm). After discretization, the  
295 resulting set of ordinary differential equations was integrated using the stiff equation solver  
296 *vode* implemented in R through the *deSolve* package (Soetaert et al. 2010b).

297 The goal of this modelling exercise was to find the mineralization rate which best fit  
298 the measured concentration depth profiles of  $NH_4^+$  and  $A_T$ . In a first step, the 10% O<sub>2</sub>  
299 treatment was analyzed (which did not show e-SOx activity – see discussion below). The  
300 mineralization rate  $R_{min}$  was determined from the best fit to the measured  $NH_4^+$  depth profile  
301 data, while  $\gamma_{CN}$  was determined from the best fit to the  $A_T$  depth profile (adopting the  $R_{min}$   
302 from the  $NH_4^+$  profile). In the remaining treatments (which did show e-SOx activity), we  
303 followed a slightly different procedure. This was because cable bacteria have been shown to  
304 impact the alkalinity of the pore water, but not the ammonium concentrations (Meysman et al.  
305 2015; Rao et al. 2016; van de Velde et al. 2016).  $R_{min}$  was first calibrated based on the  
306 measured ammonium profiles, and subsequently,  $R_{min}$  was calibrated a second time using the  
307 alkalinity depth profiles (while using the  $\gamma_{CN} = 6.4$  from the 10% O<sub>2</sub> treatment).

308 The quality of the model fit to the data was quantified by the sum of squared errors  
309 (eq. 1.4) following Berg et al. (1998).

310

311 (1.4) 
$$SSE = \sum_{i=1}^N (C_{N,i} - \bar{C}_{m,i})^2$$

312

313 where N is the number of points in the measured concentration depth profile,  $C_i$  is the  
314 measured concentration of the solute at a given sediment horizon, and  $\bar{C}_i$  is the model  
315 predicted concentration (averaged over the same depth layer where the concentration was  
316 measured). All further statistical analyses were conducted in the R software.

## 317 **Results**

### 318 **Microsensor depth profiles**

319 Initially (i.e. after 2 days of incubation), a similar set of microsensor depth profiles (pH, H<sub>2</sub>S  
320 and O<sub>2</sub>) was recorded in all treatments (Fig.2). In all treatments, ΣH<sub>2</sub>S concentrations  
321 increased steeply right below the oxygen penetration depth. The slope of the ΣH<sub>2</sub>S  
322 concentration profile was similar, suggesting high and similar rates of sulfate reduction in all  
323 treatments. The oxygen penetration depth (OPD) into the sediment was generally small and  
324 increased with increased oxygen concentration in the overlying water. Oxygen penetrated up  
325 to  $3 \pm 0.2$  mm in the 100% O<sub>2</sub> treatment, but only extended  $0.4 \pm 0.04$  mm depth in the 10%  
326 treatment. The difference between the pH of the overlying water and the asymptotic pH at  
327 depth in the sediment decreased with decreasing O<sub>2</sub> availability.

328 Starting from roughly similar initial conditions, the geochemistry subsequently  
329 developed in different ways in the four treatments. Electrogenic sulfur oxidation (e-SOx)  
330 imposes a characteristic fingerprint upon the pore water in surface sediments (Meysman et al.  
331 2015). From day 16 onwards, this fingerprint was discernable in the 100% O<sub>2</sub> treatment, as  
332 indicated by a pH maximum (pH<sub>max</sub> =  $8.35 \pm 0.04$ ) in the oxic zone of the sediment, the  
333 presence of a suboxic zone ( $\Delta L = 2.6 \pm 1.5$  mm), and the development of acidic conditions in

334 the lower part of the suboxic zone ( $\text{pH}_{\text{min}} = 6.7$ ). In the 40%  $\text{O}_2$  treatment, a similar set of  
335 microsensor depth profiles was recorded, though after 39 days of incubation. Although less  
336 pronounced than in the 40% and 100% treatments, the characteristic fingerprint of e-SOx was  
337 also detected in the 20%  $\text{O}_2$  treatment after 39 days. Even though the pH maximum in the  
338 oxic zone remained small or was absent, the development of a pronounced suboxic zone ( $\Delta L$   
339  $= 6.9 \pm 3.4$  mm) as well as the acidification of the suboxic zone points towards cable bacteria  
340 activity - see discussion in Burdorf et al. (2016); van de Velde et al. (2016) on the absence of  
341 pH maxima in electrogenic sediments. In contrast, in the 10%  $\text{O}_2$  treatment, no suboxic zone  
342 developed and no notable pH excursions were detected over the 109 days of the experiment.  
343 The pH profile remained constant with depth at each time point.

344 The differential development of e-SOx in the various treatments is illustrated by the  
345 magnitude of the suboxic zone ( $\Delta L$ ), the amplitude of the pH excursion ( $\Delta\text{pH}$ ) and the  
346 dissolved oxygen uptake rate (Fig.3). Overall, the temporal evolution of  $\Delta\text{pH}$  was similar in  
347 the three treatments that revealed cable bacteria activity (100%, 40% and 20%), and showed  
348 two consecutive phases:  $\Delta\text{pH}$  initially increased to a maximum value, after which it stabilized  
349 throughout the rest of the incubation. However, the timing of these two phases varied  
350 markedly between treatments. In the 100%  $\text{O}_2$  treatment, the maximum in  $\Delta\text{pH}$  was reached  
351 earliest (at day 25) and attained the highest value ( $\Delta\text{pH} = 1.9 \pm 0.05$ ), while in the 40% ( $\Delta\text{pH}$   
352  $= 1.2 \pm 0.04$  at day 39) and 20% ( $\Delta\text{pH} = 0.7 \pm 0.08$  at day 52) treatments, the pH excursion  
353 developed slower and remained smaller. The temporal development of the suboxic  $\Delta L$  zone  
354 also differed between treatments, and was congruent with the temporal evolution of the pH  
355 excursion. In the 100% treatment, a fast increase to  $\Delta L = 12 \pm 5$  mm was noted after 25 days,  
356 followed by a small decrease ( $\Delta L = 6.0 \pm 0.9$  mm at day 52) and a subsequent increase to a  
357 maximum of  $\Delta L = 16 \pm 4$  mm at the end of the experiment. Strikingly, the largest suboxic  
358 zone was obtained in the 40% treatment. Here, the suboxic zone first rapidly increased (day

359 39;  $\Delta L = 14 \pm 1$  mm), followed by a period of more gradual increase (day 69;  $\Delta L = 16 \pm 4$   
360 mm) to reach a maximum at the end of the incubation ( $\Delta L = 24 \pm 3$  mm). In the 20%  
361 treatment, the largest extent of the suboxic zone was measured after 52 days ( $\Delta L = 9.5 \pm 3$   
362 mm), after which it decreased again to  $5.0 \pm 0.5$  mm. Overall, the dissolved oxygen uptake  
363 (DOU, Fig 3c) was higher in the treatments with elevated oxygen levels. In all treatments the  
364 highest DOU was obtained at the start of the experiment (day 0), which is likely due to a  
365 transient increase in the  $O_2$  consumption after sediment homogenization, where a reduced  
366 layer at the surface is progressively oxidized. In the 100% treatment the DOU remains high  
367 during the initial period of  $\Delta pH$  increase (from  $31 \pm 4$   $\text{mmol m}^{-2} \text{d}^{-1}$  at day 0 to  $30 \pm 0.5$  at day  
368 25; Fig.3a). After that, the DOU decreases to attain a minimum value of  $12 \pm 2$   $\text{mmol m}^{-2} \text{d}^{-1}$   
369 at day 109. The DOU in the 40% treatment also decreases over time, while that in 10%, and  
370 20% treatments remains relatively constant throughout the time series. Note that the  
371 sediments showed a very shallow oxygen penetration (as low as 200  $\mu\text{m}$  in the 10%  
372 treatment), and so the  $O_2$  depth profiles contain only a limited number of datapoints, which  
373 increases the uncertainty on the calculated diffusive oxygen uptake (DOU).

374

### 375 **Cable bacteria abundances and morphotype**

376 The integrated abundance of the cable bacteria over depth was similar in the three treatments  
377 that developed e-SOx ( $430 - 530$   $\text{m cm}^{-2}$ , Table 2). No cable bacteria filaments were detected  
378 in the sediment samples from the 10% treatment (Table 2), matching with the absence of the  
379 e-SOx geochemical fingerprint. The depth distribution of cable bacteria (Fig.4) was similar in  
380 the 100% and 20% treatments, with the highest abundance in the top (oxic) sediment layer  
381 (100%;  $523$   $\text{m cm}^{-3}$  and 20%;  $576$   $\text{m cm}^{-3}$ ) and a decreasing abundance with depth. In  
382 contrast, the 40% treatment showed a more even depth distribution of cable bacteria, with  
383 similar filament densities in the first 15 mm of the sediment ( $280 - 320$   $\text{m cm}^{-3}$ ). In all

384 treatments, a sharp decrease in filament densities occurred when passing from the suboxic  
385 zone into the deeper sulfidic (<10% of the total filament length per area was present below the  
386 SAD). The diameter of each cable bacteria filament was recorded and provided a mean  
387 diameter of  $0.98 \pm 0.32 \mu\text{m}$  (filament fragments inspected  $n = 351$ ). No observable  
388 differences in filament width were found between the three oxygen conditions (ANOVA;  $F =$   
389  $2.12$ ;  $df = 2$ ;  $p = 0.12$ ), yet cable bacteria in the oxic zone were significantly thinner than the  
390 cable bacteria in the anoxic zone ( $0.80 \pm 0.26 \mu\text{m}$ , vs  $1.02 \pm 0.34 \mu\text{m}$ ; Welch t-test;  $t = 6.79$ ;  
391  $df = 314.7$ ;  $p < 0.001$ ).

392

### 393 **Pore water geochemistry**

394 Concentration depth profiles of pore water constituents ( $\text{Fe}^{2+}$ ,  $\text{Mn}^{2+}$ ,  $\text{Ca}^{2+}$ ,  $\text{SO}_4^{2-}$ ,  $\text{A}_T$  and  
395  $\text{NH}_4^+$ ) were determined after 39 days of incubation in all treatments. The two replicate cores  
396 analyzed in each treatment gave similar depth profiles (Fig.5).

397 The pore water inventory of dissolved iron ( $\text{Fe}^{2+}$ ) decreased with decreasing  $\text{O}_2$   
398 availability (Fig.5a; Table 2). A clear enrichment of pore water iron was observed in the  
399 suboxic zone of the sediment in the 40% and 100%  $\text{O}_2$  treatments, with a subsurface  $\text{Fe}^{2+}$   
400 peak at 20 mm. The peak concentration of  $\text{Fe}^{2+}$  was highest in the fully oxic treatment ( $0.31$   
401  $\text{mmol L}^{-1}$ ). In the 20% treatment, dissolved iron was only detected in the top 5 mm (max  
402  $[\text{Fe}^{2+}]$ ;  $0.05 \text{ mmol L}^{-1}$ ), while in the 10% treatment, dissolved iron remained below the  
403 detection limit at all depths.

404 Dissolved manganese ( $\text{Mn}^{2+}$ ) concentrations also showed a clear trend between  
405 treatments (Fig.5b), with a decreasing inventory of  $\text{Mn}^{2+}$  with decreasing oxygen availability  
406 (Table 2). In the 100%  $\text{O}_2$  treatment,  $\text{Mn}^{2+}$  reached the highest concentration in the upper  
407 sediment layer and a small secondary  $\text{Mn}^{2+}$  peak was situated at 2 cm deep (present in both

408 replicate cores). In contrast, in the three other treatments, the  $\text{Mn}^{2+}$  profile showed one  
409 subsurface peak, which was located between 1–2 cm deep in the sediment.

410 All  $\text{Ca}^{2+}$  profiles showed a subsurface maximum (Fig.5c), indicating  $\text{CaCO}_3$   
411 dissolution within the suboxic zone, and the pore water inventory of  $\text{Ca}^{2+}$  decreased with  
412 decreasing  $\text{O}_2$  availability (Table 2). In the 100% and 40% treatments, a strong accumulation  
413 of  $\text{Ca}^{2+}$  was observed in the first 30 mm of the core, with slightly higher concentrations in the  
414 fully oxygenated cores (max.  $[\text{Ca}^{2+}]$ : 20.5  $\text{mmol L}^{-1}$ ) compared to the 40%  $\text{O}_2$  core (max.  
415  $[\text{Ca}^{2+}]$ : 18  $\text{mmol L}^{-1}$ ). Only a small enrichment was measured in the 20%  $\text{O}_2$  treatment (max.  
416  $[\text{Ca}^{2+}]$ : 14.5  $\text{mmol L}^{-1}$ ) compared to the 10% treatment (max.  $[\text{Ca}^{2+}]$ : 12.3  $\text{mmol L}^{-1}$ ).

417 The sulfate ( $\text{SO}_4^{2-}$ ) depth profiles (Fig.5d) were highly similar in all treatments and  
418 decreased from 27-30  $\text{mmol L}^{-1}$  in the top of the sediment to 10 – 12  $\text{mmol L}^{-1}$  at the bottom  
419 of the sediment cores. Alkalinity increased from 5  $\text{mmol L}^{-1}$  in the top of the sediment to 25  
420  $\text{mmol L}^{-1}$  deeper in the sediment with no real difference between treatments (Fig.5e). The  
421 ammonium concentrations (Fig.5f) were also similar in all treatments and steadily increased  
422 from 0.1  $\text{mmol L}^{-1}$  near the sediment-water interface to ~1.5  $\text{mmol L}^{-1}$  at depth.

423

#### 424 **Mineralization rates**

425 To estimate the mineralization rate in the incubated sediment cores, we implemented a  
426 simplified reactive transport model, which provided satisfactory fits to the alkalinity ( $A_T$ ) and  
427 ammonium ( $\text{NH}_4^+$ ) depth profiles in all treatments (Figure 6 and Table 3). The C:N ratio was  
428 estimated at 6.4 (fitted as described in section 2.5), which is close to the expected Redfield  
429 C:N ratio (6.6). It is slightly lower than the C:N ratio previously measured in bulk organic  
430 matter from Lake Grevelingen sediments, (7.2 in situ (Seitaj et al. 2017) and 9.0 in laboratory  
431 setup (Rao et al. 2016), which suggests preferential mineralization of nitrogen compared to  
432 carbon.

433 The model-estimated mineralization rate based on the alkalinity pore water profiles  
434 ( $\sim 34 - 39 \text{ mmol C m}^{-2} \text{ d}^{-1}$ ) fits well the values earlier reported values for sediments from the  
435 field site ( $\sim 28 \text{ mmol C m}^{-2} \text{ d}^{-1}$  at  $16^\circ\text{C}$ , Rao et al. (2016)). A slightly higher mineralization  
436 rate is obtained for the fully oxic treatment ( $39 \text{ mmol C m}^{-2} \text{ d}^{-1}$ ), but this remains close to the  
437 values computed for the other treatments ( $37 \text{ mmol C m}^{-2} \text{ d}^{-1}$  in the 40%  $\text{O}_2$  treatment,  $37.6$   
438  $\text{mmol C m}^{-2} \text{ d}^{-1}$  in the 20%  $\text{O}_2$  treatment and  $37.5 \text{ mmol C m}^{-2} \text{ d}^{-1}$  in the 10%  $\text{O}_2$  treatment).  
439 Similarly, the modelled ammonification rate is slightly higher in 100%  $\text{O}_2$  treatment ( $6.0$   
440  $\text{mmol N m}^{-2} \text{ d}^{-1}$ ) compared to the other treatments (between  $5.3 - 5.5 \text{ mmol N m}^{-2} \text{ d}^{-1}$ ).

441 Mineralization rates were estimated by a second, independent method (based on  
442 alkalinity changes in the overlying water) and these were fully consistent with the values  
443 obtained by model fitting. Total alkalinity in the reservoir water was approx.  $\sim 2.0 \text{ mM}$  at the  
444 start of the closed incubations. On Day 39, the alkalinity concentration in all treatments had  
445 similarly increased to a value of  $\sim 4.2 \text{ mM}$  (as inferred from the concentration at the sediment-  
446 water interface in the depth profile). In a closed system with a recirculation water volume of  
447  $\sim 15\text{L}$ , and which contains two sediment cores with a diameter of  $12 \text{ cm}$ , this alkalinity  
448 increase translates into an average alkalinity efflux of  $38 \text{ mmol C m}^{-2} \text{ d}^{-1}$  from the sediment to  
449 the overlying water. Assuming the sediment cores are in steady state, alkalinity efflux forms a  
450 proxy for the alkalinity production, further substantiating that our estimates for mineralization  
451 rate  $R_{\text{min}}$  obtained by model fitting are accurate.

## 452 **Discussion**

### 453 **Growth dynamics of cable bacteria in marine sediments**

454 By monitoring the imprint of e-SOx on pore water solutes (e.g. pH,  $\text{H}_2\text{S}$  and  $\text{O}_2$ ), the  
455 metabolic activity of cable bacteria can be tracked non-destructively through time, providing  
456 information on their growth and development (Schauer et al. 2014). In the fully oxygenated  
457 treatment, we observed substantial e-SOx activity within 16 days (Fig.2), indicating that a

458 sizeable and active population of cable bacteria had developed. This confirms observations  
459 from previous laboratory enrichment experiments, where the first detectable sign of cable  
460 bacteria activity is typically observed after 5-14 days, depending on incubation temperature  
461 (Schauer et al. 2014; Vasquez-Cardenas et al. 2015; Rao et al. 2016). These observations  
462 confirm that cable bacteria are fast growing, and thus capable of rapidly establishing long-  
463 distance electron transport in the surface layer of aquatic sediments (Pfeffer et al. 2012). At  
464 the same time, the metabolic activity of cable bacteria has a large impact on the sediment  
465 through an increase in oxygen consumption, the depletion of the sulfide in the first  
466 centimeters of the sediment, and via intense pore water acidification ( $>1.5$  pH units, e.g.  
467 Vasquez-Cardenas et al. 2015; Burdorf et al. 2017; Fig. 2). The fast growth dynamics of cable  
468 bacteria allows drastic shifts in the geochemical cycling of aquatic sediments over short time  
469 intervals (on the order of days to weeks), thus creating the possibility of rapid transient  
470 changes in sediment geochemistry. This has important consequences for the interpretation and  
471 analysis of sediment geochemistry data, which is at present largely dominated by a steady-  
472 state perspective (Boudreau 1997).

473         The results obtained here are in line with previous laboratory enrichments, which  
474 suggest that the development of cable bacteria population includes four consecutive periods: a  
475 lag phase, an exponential growth phase, a steady-state plateau and a final senescence phase  
476 (Schauer et al. 2014; Vasquez-Cardenas et al. 2015; Burdorf et al. 2017). The lag phase  
477 includes several days without notable signs of e-SO<sub>x</sub> activity (no suboxic zone is present and  
478 no acidification of the subsurface is detected); in the period of exponential growth, e-SO<sub>x</sub>  
479 activity becomes detectable and rapidly increases (the sulfide appearance depth deepens fast,  
480 e.g. 1 cm over 3 days, Burdorf et al. (2017) and pH excursions become apparent); in the  
481 subsequent period of stabilization, e-SO<sub>x</sub> activity becomes constant; the expansion of the  
482 suboxic zone is halted and the pH profile remain more or less stable; finally, in the period of

483 decline, e-SOx activity gradually fades (the pH excursions in the pore water become smaller  
484 and the sulfide again moves upwards towards the sediment-water interface).

485 In our experiment, we quantified this temporal pattern by tracking the extent of the  
486 suboxic zone  $\Delta L$  and the acidification excursion  $\Delta pH$  (Fig.3 a-b). Both these quantities are  
487 indicators for the intensity of the metabolic activity of cable bacteria. The width of the  
488 suboxic zone  $\Delta L$  is governed both by the intensity of cathodic oxygen reduction  
489 ( $O_2 + 4e^- + 4H^+ \rightarrow 2H_2O$ ), which decreases the oxygen penetration depth, and by  
490 anodic sulfide oxidation ( $H_2S + 4H_2O \rightarrow SO_4^{2-} + 8e^- + 10H^+$ ), which increases the  
491 sulfide appearance depth. Similarly, the value of  $\Delta pH$  is governed by proton consumption  
492 near the sediment-water interface due to cathodic oxygen reduction and proton production at  
493 depth resulting from anodic sulfide oxidation.

494 The treatments which developed an active cable bacteria population (100%, 40% and  
495 20%  $O_2$ ) all proceeded through a similar development pattern, which roughly fits the four-  
496 phase pattern described above. All three treatments first showed an exponential growth phase,  
497 after which the e-SOx activity peaked and subsequently declined again (Fig.3a-b). The lag  
498 phase was not as clear as in previous studies, likely because the time resolution of  
499 microsensor profiling in the initial stage of our experiment was rather coarse. Similarly, the  
500 decline phase as observed here was not as pronounced as in previous studies (the  $\Delta pH$  goes  
501 through a maximum, and the suboxic zone  $\Delta L$  also goes through a maximum, but then  
502 increases again in the 100% and 40% treatments). Overall, the growth dynamics of cable  
503 bacteria seems to be of a boom-and-bust nature, i.e., a fast development towards maximal  
504 activity followed by subsequent decline.

505 It should however be noted that this growth pattern has always been observed after a  
506 disturbance event. In the laboratory enrichment experiments conducted until present, this  
507 disturbance event involves an initial “reset” of the geochemistry, either through sediment

508 mixing or through sediment asphyxiation, and subsequently re-exposing the sediment to an  
509 oxygenated overlying water column. Natural analogues of such a sediment disturbance are  
510 likely erosion-resuspension events or the development of bottom water hypoxia. Yet, it is not  
511 clear at present how important these disturbance events for the natural distribution of cable  
512 bacteria. Currently, only a few studies have documented the temporal dynamics of cable  
513 bacteria populations under natural conditions (Seitaj et al. 2015; van de Velde et al. 2016;  
514 Malkin et al. 2017), and these studies do not yet enable general conclusions on the natural  
515 growth dynamics of cable bacteria. It hence remains unclear whether cable bacteria have an  
516 ephemeral and opportunistic lifestyle (i.e. they grow in a boom-bust fashion after a sediment  
517 disturbance), or whether than they can establish continuous populations for long time within  
518 aquatic sediments.

519

#### 520 **Sulfur cycling in electro-active sediments**

521 Cable bacteria have been shown to thrive in a large number of coastal marine habitats  
522 worldwide (Malkin et al. 2014; Burdorf et al. 2017). A common factor of these habitats (i.e.  
523 mangrove sediments, intertidal mud flats, bivalve reefs) are the high rates of sulfate reduction,  
524 which results in high rates of free sulfide production, and hence a large pool of reduced sulfur  
525 compounds in the top centimeters of the sediment (e.g. free sulfide, elemental sulfur, iron  
526 sulfides, pyrite). Cable bacteria appear to mainly – or even exclusively - utilize free sulfide  
527 ( $H_2S$ ) as the electron donor in anodic sulfide oxidation (Nielsen and Risgaard-Petersen 2015).  
528 Sulfide consumption is thought to take place throughout the suboxic zone, and free sulfide is  
529 supplied in three principle ways to the cable bacteria (Meysman et al. 2015; Fig.7). Firstly,  
530 free sulfide is produced in deeper sediment layers by sulfate reduction, and generates a  
531 diffusive flux upwards to the suboxic zone. This free sulfide is consumed by the cable  
532 bacteria at or just below the sulfide appearance depth. Secondly, iron sulfides (FeS) are

533 dissolving within the suboxic zone, as a result of the acidification induced by anodic sulfide  
534 oxidation (here ~ 2 pH units on Day 23 in the 100% O<sub>2</sub> treatment, Fig.3a). Iron sulfide  
535 dissolution releases free sulfide to the pore water ( $FeS + H^+ \rightarrow Fe^{2+} + HS^-$ ), which is then  
536 consumed by the cable bacteria. Note this creates a positive feedback loop, where a higher  
537 metabolic activity of cable bacteria induces a higher acidity of the pore water, which then  
538 stimulates FeS dissolution and free sulfide release, but also again sustains a higher metabolic  
539 activity (Meysman et al. 2015). A third source of free sulfide is due to sulfate reduction within  
540 the suboxic zone. Because sulfide is depleted below detection limit within the suboxic zone,  
541 this gives rise to a cryptic sulfur cycle, where the free sulfide produced by sulfate reduction is  
542 immediately scavenged and oxidized by the cable bacteria. Model simulations reveal that  
543 cable bacteria must have a high affinity for free sulfide in order to keep the free sulfide  
544 concentration to below detection limit (Meysman et al. 2015).

545         We examined the relative importance of the three supply pathways by establishing a  
546 sedimentary budget for sulfur and iron. This mass balance procedure was applied to all four  
547 treatments on Day 39. The procedure delineates three biogeochemical zones (oxic zone,  
548 suboxic zone and sulfidic zone), and it is assumed that the activity of cable bacteria is  
549 restricted to the suboxic zone. Fluxes and reaction rates are shown in Table 3 and Figure 7  
550 (see the caption of Table 3 for the calculation procedure). The sulfur budget reveals that  
551 sulfate reduction is the most important source of sulfide to the cable bacteria (Table 3). Most  
552 is coming from sulfate reduction in deeper layers (67-82% of the sulfide supply), while a  
553 smaller amount (18-20 %) is coming from sulfate reduction within the suboxic zone itself. In  
554 the 100% O<sub>2</sub> treatment, FeS dissolution amounts to 2.5 mmol m<sup>-2</sup> d<sup>-1</sup>, which equals 12% of  
555 the total free sulfide supplied to the suboxic zone. In the 40% O<sub>2</sub> treatment, the share of FeS  
556 dissolution is even less (5% or 1.0 mmol m<sup>-2</sup> d<sup>-1</sup> or), while all sulfide in the 20% treatment  
557 stems from sulfate reduction and no dissolution of FeS was observed (Fig.5). Previous studies

558 attribute a markedly higher share of the sulfide used in e-SOx to FeS-dissolution. During  
559 incubation of Baltic sea sediments, recovered in Aarhus Bay, Risgaard-Petersen et al. (2012)  
560 found that almost all sulfide used in e-SOx originated from FeS-dissolution (94%). A field  
561 study on a subtidal mud bank in Belgium (van de Velde et al. 2016) calculated a smaller share  
562 of FeS in sulfide production for e-SOx (37%). Accordingly, the fueling of e-SOx via FeS  
563 dissolution seems to be highly variable between environments.

564         The absence of transient sulfide accumulation in the pore water and the persistence of  
565 a suboxic zone indicates that e-SOx must consumes all the free sulfide that is produced in the  
566 sediment. Since sulfate reduction rates are high in our sediments (Table 3), e-SOx rates are  
567 also high ( $17.8 \text{ mmol S m}^{-2} \text{ d}^{-1} - 20.9 \text{ mmol S m}^{-2} \text{ d}^{-1}$ ; Table 3) and substantially exceed the  
568 rates obtained in previous studies ( $3.3 \text{ mmol S m}^{-2} \text{ d}^{-1} - 7.3 \text{ mmol S m}^{-2} \text{ d}^{-1}$ ; Risgaard-Petersen  
569 et al. 2012; van de Velde et al. 2016). In theory, the rates of anoxic sulfide oxidation and  
570 cathodic oxygen reduction must be coupled through an electron balance. However, the DOU  
571 values obtained were far too low to match the estimated sulfide consumption via e-SOx  
572 (assuming that all sulfide is oxidized to sulfate). To balance the predicted  $18 - 21 \text{ mmol m}^{-2} \text{ d}^{-1}$   
573 <sup>1</sup> of anodic sulfide removal (Table 3), a cathodic O<sub>2</sub> uptake rate of  $36 - 42 \text{ mmol m}^{-2} \text{ d}^{-1}$  would  
574 be needed. The estimated DOU values are however much lower ( $7 - 16 \text{ mmol m}^{-2} \text{ d}^{-1}$ , Table  
575 3). There are a number of ways to explain this. A first possibility is that part of the free sulfide  
576 produced by sulfate reduction is not re-oxidized, and hence, some free sulfide diffuses out of  
577 the sediment. While this could be occurring in the 10% O<sub>2</sub> treatment, it is excluded in all other  
578 treatments, because a suboxic zone formed, which implies that all free sulfide in the sediment  
579 must be effectively reoxidized. A second possibility is that all sulfide is oxidized, but not all  
580 the way up to sulfate, thus producing sulfur compounds with an intermediate oxidation state,  
581 like elemental sulfur or thiosulfate. For example, if anodic sulfide oxidation would only  
582 produce elemental sulfur, ( $H_2S + 4H_2O \rightarrow S^0 + 2e^- + 2H^+$ ), then the corresponding

583 DOU range would become  $9 - 10.5 \text{ mmol m}^{-2} \text{ d}^{-1}$ , which matches the estimated range.  
584 However, this would imply that substantial amounts of elemental sulfur would accumulate in  
585 the sediment. Although no solid phase analysis was performed, we have no indications (e.g.  
586 sediment discoloration) for such an accumulation of elemental sulfur. Another option is that  
587 the cathodic oxygen reduction is underestimated. This could occur when cable bacteria not  
588 only access the oxygen within the sediment core, but that part of their filament sticks out of  
589 the sediment to directly consume  $\text{O}_2$  in the water column. This way of oxygen consumption  
590 would not be reflected in our  $\text{O}_2$  depth profiles and DOU values.

591 To test whether cable bacteria access the oxygen directly in the water column, we set  
592 up a new small sediment incubation experiment. To this end, small transparent sediment  
593 chambers (height: 50 mm; width: 10mm; depth: 2mm) were constructed (Fig.8) , which were  
594 dug into the sediment, level with the sediment-water interface. The chambers were incubated  
595 for 16 days with two oxygen levels in the overlying water (i.e.  $268 \mu\text{mol L}^{-1}$  and  $160 \mu\text{mol L}^{-1}$ ,  
596 corresponding to 100% and 50%  $\text{O}_2$  saturation). At the end of the incubation period, the  
597 glass chambers were retrieved from the sediment, washed and inspected by microscopy. This  
598 experiment showed numerous cable bacteria filaments sticking out of the sediment in the  
599 lower oxygen treatment, while no cables were seen sticking out at the higher oxygen  
600 treatment (Fig. 8). Accordingly, at reduced  $\text{O}_2$  concentrations, the cable bacteria appear to  
601 extend from the sediment, in order to harvest  $\text{O}_2$  within the diffusive boundary layer above the  
602 sediment. This way, their oxygen consumption would occur above the sediment-water  
603 interface, and hence will not be accounted for in the DOU (which is only based on  $\text{O}_2$   
604 data below the sediment-water interface).

### 605 **Metabolic activity of cable bacteria and $\text{O}_2$ availability**

606 Our experiments here provide the first insight into this oxygen dependence of  
607 electrogenic sulfur oxidation. Conspicuously, the time interval over which the cable bacteria

608 developed in our sediment incubations was dependent on the oxygen availability. Based on  
609  $\Delta\text{pH}$  (Fig.3a), we observed a shorter exponential growth phase in the fully oxic treatment (i.e.  
610 from day 2 to day 25) in contrast to the 20% treatment (Fig.2, Fig.3). The time point of  
611 maximum cable bacteria intensity (as defined by the maximum in  $\Delta\text{pH}$ ) was reached on Day  
612 25 in the 100% treatment, on Day 39 in the 40% treatment and on Day 52 in the 20%  
613 treatment. Similarly, the width of the suboxic zone (Fig.3b) increased to a maximum within  
614 25 days in the 100% treatment (to 1.5 cm in 25 days), while this took 39 days in the 40%  
615 treatment and up to 58 days in the 20% treatment.

616 The population dynamics suggests a slower development in the lower oxygen  
617 treatments (Fig.2, Fig.3), while the sulfur and iron budgets also show a lower anodic sulfide  
618 oxidation at day 39 (Table 3). Our time series provide various lines of evidence for the idea  
619 that the rate of e-SO<sub>x</sub> decreases when the O<sub>2</sub> levels in the overlying water decreases (Fig.2).  
620 Firstly, higher e-SO<sub>x</sub> rates would cause higher oxygen uptake rates. Despite the relative large  
621 uncertainty, the DOU values obtained from our time series experiments show a clear  
622 decreasing trend with O<sub>2</sub> availability, with systematically lower DOU values in the 20% and  
623 40% oxygen treatments (Fig.3c). Second, when the metabolic activity of the cable bacteria  
624 increases, one expects the associated pH excursions to also increase. Through increased rates  
625 of anodic sulfide oxidation, leading to increased proton production at depth, and increased  
626 cathodic oxygen reduction, leading to higher proton consumption rates near the sediment  
627 interface, one obtains a larger  $\Delta\text{pH}$  excursion. Our data suggest that higher O<sub>2</sub> availability  
628 indeed leads to higher  $\Delta\text{pH}$  values (Fig.3a). The highest  $\Delta\text{pH}$  was reached in the 100% (1.9,  
629 day 25), followed by the 40% (1.3, day 39). Thirdly, when the metabolic activity of the cable  
630 bacteria increases, one expects a higher accumulation of cations in the pore water. This is  
631 because the metabolic activity of cable bacteria has a large effect on the geochemistry of the  
632 sediment, through its impact on pH (Risgaard-Petersen et al. 2012; Meysman et al. 2015; Rao

633 et al. 2016), which is a geochemical “master variable” (Stumm and Morgan 1981). Laboratory  
634 experiments (Risgaard-Petersen et al. 2012; Rao et al. 2016), field measurements (Seitaj et al.  
635 2015; van de Velde et al. 2016) and modelling (Meysman et al. 2015) have shown that the  
636 acidification induced by e-SOx leads to the dissolution of acid-sensitive minerals, such as FeS  
637 and CaCO<sub>3</sub>, in the suboxic zone.

638         On Day 39 of the incubation, the total inventories of remobilized cations Fe<sup>2+</sup>, Ca<sup>2+</sup>  
639 and Mn<sup>2+</sup> are larger with higher O<sub>2</sub> availability (Table 2), indicating mobilization of Fe<sup>2+</sup>  
640 through the dissolution of FeS (Fig.5a), of Ca<sup>2+</sup> through the dissolution of CaCO<sub>3</sub> (Fig.5c) and  
641 of Mn<sup>2+</sup> likely associated to FeS and CaCO<sub>3</sub> minerals (van de Velde et al., 2017; Fig.5b). This  
642 hence suggests that increased e-SOx activity leads to increased acidification of the suboxic  
643 zone, thus stimulating the dissolution of acid-sensitive minerals. However, it should be noted  
644 that our pore water analyses only provided a snapshot of the sediment geochemistry at a  
645 single time point (i.e. on Day 39 of the incubation). Cable bacteria induce a transient  
646 development of the geochemical cycling in the sediment. As noted above, this transient  
647 development occurred at different “speeds” in the different treatments (Fig.3). The large  
648 remobilization of Fe<sup>2+</sup>, Mn<sup>2+</sup> and Ca<sup>2+</sup> are primarily dependent on absolute minimum pH  
649 reached in the pore water. In all treatments with cable bacteria, the pH minimum reached  
650 similar levels over time (6.1 – 6.3) and would enable a similar dissolution of e.g. CaCO<sub>3</sub> and  
651 FeS in all treatments.

652         In contrast to the higher activity of cable bacteria derived from the geochemistry, the  
653 quantification of the cable bacteria at day 39 (Fig.4) shows a similar length density of cable  
654 bacteria between the 20%, 40% and 100%. Accordingly, the difference in e-SOx activity at  
655 day 39 between treatments is contradicted by the counts of cable bacteria (Fig.4, Table 2).  
656 The integrated length density of the cable bacteria (~ 430 – 530 m cm<sup>-2</sup>) did not vary  
657 systematically between treatments. The density of cable bacteria is related not only to the

658 activity of the cable bacteria, but is also a result of the population dynamics. At the time of  
659 slicing cable bacteria activity was already decreasing in the 100% treatment, while the cable  
660 bacteria activity was still increasing in the 20% and 40% treatment.

661 Lower oxygen availability thus seems to decrease the activity of the cable bacteria,  
662 and delay the effect of e-SO<sub>x</sub> on the sediment geochemistry. The growth of cable bacteria in a  
663 sediment covered with a photosynthetic biofilm (Malkin and Meysman 2015), raises the  
664 question whether the opposite also holds true (faster growth, faster acidification with more  
665 O<sub>2</sub>). In such environments O<sub>2</sub> saturation surpasses 100% and could induce an even faster  
666 acidification of the suboxic zone through e-SO<sub>x</sub>.

667

#### 668 **The oxygen limit of electrogenic sulfur oxidation**

669 The present model on the environmental conditions controlling cable bacteria growth  
670 is based on three main assumptions. Firstly, a sufficient amount of a suitable electron acceptor  
671 must be present. In our experiments we find that cable bacteria develop when at least 50 μmol  
672 L<sup>-1</sup> O<sub>2</sub> (20% treatment, Fig.2, Fig.4) is available. Alternatively, cable bacteria can use nitrate  
673 as an electron acceptor (tested with >200 μmol L<sup>-1</sup> in laboratory setup, Marzocchi et al. 2014),  
674 but in this study, the use of nitrate by cable bacteria was minimized by incubating the  
675 sediment in low nutrient seawater ([NO<sub>3</sub>] < 0.1 μmol L<sup>-1</sup>). The second requirement for cable  
676 bacteria growth is the availability of an electron-donor (H<sub>2</sub>S). Finally, cable bacteria activity  
677 is proposed to be limited by the physical disturbance of the filament-network by bioturbators  
678 (Pfeffer et al. 2012; Malkin et al. 2014; Rao et al. 2014). But recent findings indicate that the  
679 control of bioturbation on cable bacteria distribution might be less efficient than previously  
680 thought (Malkin et al. 2017; Burdorf et al. 2017).

681 If we apply these conditions – at least 50 μmol L<sup>-1</sup> O<sub>2</sub>, and sufficient H<sub>2</sub>S availability–  
682 onto the modern oceans, possible habitats for cable bacteria are present across a vast depth

683 range. Sulfate reduction is predominately present on the continental shelf and slope (e.g.  
684 >80% of global sulfate reduction is limited to 1000m water depth (Jørgensen and Kasten  
685 2006; Bowles et al. 2014), although local deep-sea “hotspots” exist. These sites in the deep-  
686 sea with significantly higher sulfate reduction have a supplemental source of either methane  
687 (cold seeps), sulfur (hydrothermal vents) or organic matter (carcasses).

688         With sufficient sulfide available, the cable bacteria distribution on the continental  
689 slope and shelf is most likely to be limited by oxygen availability and bioturbation. Although  
690 the majority of the oceans are fully oxic, oxygen depletion is globally increasing (Diaz and  
691 Rosenberg 2008). Human-impacted coastal systems, where additional nutrients run-off into  
692 the marine waters from land, are increasingly enduring (seasonal) oxygen depletion. Cable  
693 bacteria are present and active in these seasonal hypoxic systems, but e-SO<sub>x</sub> activity has only  
694 been measured during periods with high oxygen levels (Seitaj et al. 2015; Burdorf et al.  
695 2017). Apart from coastal regions, oxygen depletion also occurs naturally in productive,  
696 typically upwelling region of the oceans. These so-called oxygen minimum zones  
697 (abbreviated as OMZ) are persistent features in productive oceanic regions with high  
698 upwelling rates. Although there is a large geographical variability to the extent of these  
699 oxygen deficient water layers, OMZ waters are usually found between 100 – 1800 m deep in  
700 the bathyal zone (Gallo and Levin 2016). Sediments under these oxygen deficient waters are  
701 usually organic carbon rich, sulfidic (Middelburg and Levin, 2009) and typically harbor big  
702 sulfide oxidizing bacteria like *Thioploca* and *Beggiatoa*. Although species of cable bacteria  
703 have been described which are able to use nitrate as an alternative electron donor, the high  
704 concentrations of these incubations (>200 μmol L<sup>-1</sup> NO<sub>3</sub>) and the fact that cable bacteria  
705 likely cannot accumulate nitrate, leaves the questions open whether this process actually can  
706 occur within the OMZ. On the continental rise however, the sediment is covered by waters of  
707 varying oxygen concentrations, as it crosses through the upper and lower boundary of the

708 oxygen minimum zones. Also termed as oxygen limited zones (Gilly et al. 2013), an  
709 important oxygen gradient is present in these zones. Here, cable bacteria might benefit from  
710 an absence of large bioturbators and just enough oxygen to develop.

711         The O<sub>2</sub> availability can also be used to speculate about a geological timeframe when e-  
712 SO<sub>x</sub> first developed. Although, the scientific debate on oceanic oxygen concentrations is still  
713 open (Lyons et al. 2014), the first “whiffs” of oxygen produced by cyanobacteria are placed in  
714 the Archeon eon around 3 Ga years ago (Anbar et al. 2007). The extensive presence of  
715 reductive materials in the atmosphere as well as in the oceans however prevented substantial  
716 oxygen accumulation. The first great oxidation event (GOE) on the border of the Archeon and  
717 the Proterozoic eon (2.54 Ga) led to the first accumulation in oxygen to 10<sup>-4</sup> – 10<sup>-1</sup> of present  
718 levels in the atmosphere (Lyons et al. 2014). However oxygen is not hypothesized to have  
719 reached the bottoms of the oceanic basins at that time, which are thought to still have been  
720 euxinic (sulfidic, Canfield (1998)) or ferruginous (iron-rich). Whether e-SO<sub>x</sub> could have  
721 developed within this timeframe would rely on the spatial heterogeneity in oxygen  
722 concentrations. Given the large anoxic past of the earth’s sediment, the electron donor  
723 (sulfide) would have been ample available, and the evolution of large bioturbators did not yet  
724 start. One could imagine that an intertidal area with a cyanobacteria mat on the sediment  
725 could have created the environment needed for cable bacteria development. During the second  
726 oxidation event (~0.54 Ga) oxygen rose up to present levels. The sufficient oxygen  
727 concentrations throughout the oceans and the absence of bioturbators at the start of the  
728 oxidation may have created the ideal conditions for the widespread evolution of e-SO<sub>x</sub>.

729  
730 *Acknowledgements*

731 We thank the analytical laboratory of NIOZ Yerseke for their support during the pore water  
732 analyses. We additionally thank Silvia Hidalgo-Martinez for the guidance and support of  
733 Francis Criens during the FISH-analysis. This research was financially supported by the

734 European Research Council under the European Union's Seventh Framework Programme  
735 (FP/2007-2013) through ERC Grant 306933 to FJRM and JTB was funded through ERC  
736 grant 291650, and by the Research Foundation Flanders via FWO grant G031416N to FJRM.  
737

738 **References**

- 739 Aminot, A., R. K  rouel, and S. C. Coverly. 2009. Nutrients in seawater using segmented flow  
740 analysis., p. 143–178. *In* O. Wurl [ed.], Practical guidelines for the analysis of  
741 seawater. CRC Press.
- 742 Anbar, A. D., Y. Duan, T. W. Lyons, and others. 2007. A whiff of oxygen before the great  
743 oxidation event? *Science* **317**: 1903–1906. doi: 10.1126/science.1140325
- 744 Berg, P., N. Risgaard-Petersen, and S. Rysgaard. 1998. Interpretation of measured  
745 concentration profiles in sediment pore water. *Limnol. Oceanogr.* **43**: 1500–1510.  
746 doi:10.4319/lo.1998.43.7.1500
- 747 Boudreau, B. P. 1997. Diagenetic models and their implementation, Springer Berlin.
- 748 Bowles, M. W., J. M. Mogoll  n, S. Kasten, M. Zabel, and K.-U. Hinrichs. 2014. Global rates  
749 of marine sulfate reduction and implications for sub–sea-floor metabolic activities.  
750 *Science* **344**: 889–891. doi:10.1126/science.1249213
- 751 Burdorf, L. D. W., S. Hidalgo-Martinez, P. L. M. Cook, and F. J. R. Meysman. 2016. Long-  
752 distance electron transport by cable bacteria in mangrove sediments. *Mar. Ecol. Prog.*  
753 *Ser.* **545**: 1–8. doi:10.3354/meps11635
- 754 Burdorf, L. D. W., A. Tramper, D. Seitaj, L. Meire, S. Hidalgo-Martinez, E.-M. Zetsche, H.  
755 T. S. Boschker, and F. J. R. Meysman. 2017. Long-distance electron transport occurs  
756 globally in marine sediments. *Biogeosciences* **14**: 683–701. doi:10.5194/bg-14-683-  
757 2017
- 758 Canfield, D. E. 1998. A new model for Proterozoic ocean chemistry. *Nature* **396**: 450–453.  
759 doi:10.1038/24839
- 760 Diaz, R. J., and R. Rosenberg. 2008. Spreading Dead Zones and Consequences for Marine  
761 Ecosystems. *Science* **321**: 926–929. doi:10.1126/science.1156401
- 762 Dickson, A. G., C. L. Sabine, and J. R. Christian. 2007. Guide to Best Practices for Ocean  
763 CO2 Measurements. Report North Pacific Marine Science Organization.

- 764 Gallo, N. D., and L. A. Levin. 2016. Fish Ecology and Evolution in the World's Oxygen  
765 Minimum Zones and Implications of Ocean Deoxygenation, p. 117–198. *In* B.E.  
766 Curry [ed.], *Advances in Marine Biology*. Academic Press.
- 767 Gilly, W. F., J. M. Beman, S. Y. Litvin, and B. H. Robison. 2013. Oceanographic and  
768 Biological Effects of Shoaling of the Oxygen Minimum Zone. *Annu. Rev. Mar. Sci.* **5**:  
769 393–420. doi:10.1146/annurev-marine-120710-100849
- 770 Hofmann, A. F., K. Soetaert, J. J. Middelburg, and F. J. R. Meysman. 2010. AquaEnv: An  
771 Aquatic Acid–Base Modelling Environment in R. *Aquat. Geochem.* **16**: 507–546.  
772 doi:10.1007/s10498-009-9084-1
- 773 Jørgensen, B. B. 1982. Mineralization of organic matter in the sea bed—the role of sulphate  
774 reduction. *Nature* **296**: 643–645. doi:10.1038/296643a0
- 775 Jørgensen, B. B., and S. Kasten. 2006. Sulfur cycling and methane oxidation, p. 271–309. *In*  
776 *Marine geochemistry*. Springer.
- 777 Kristensen, E., S. Bouillon, T. Dittmar, and C. Marchand. 2008. Organic carbon dynamics in  
778 mangrove ecosystems: A review. *Aquat. Bot.* **89**: 201–219.  
779 doi:10.1016/j.aquabot.2007.12.005
- 780 Lyons, T. W., C. T. Reinhard, and N. J. Planavsky. 2014. The rise of oxygen in Earth's early  
781 ocean and atmosphere. *Nature* **506**: 307–315. doi:10.1038/nature13068
- 782 Malkin, S., D. Seitaj, L. Burdorf, and others. 2017. Electrogenic sulfide oxidation by cable  
783 bacteria in bivalve reef sediments. *Front. Mar. Sci.* **4**. doi:10.3389/fmars.2017.00028
- 784 Malkin, S. Y., and F. J. R. Meysman. 2015. Rapid redox Signal transmission by “Cable  
785 Bacteria” beneath a photosynthetic biofilm. *Appl. Environ. Microbiol.* **81**: 948–956.  
786 doi:10.1128/AEM.02682-14
- 787 Malkin, S. Y., A. M. Rao, D. Seitaj, D. Vasquez-Cardenas, E.-M. Zetsche, S. Hidalgo-  
788 Martinez, H. T. Boschker, and F. J. Meysman. 2014. Natural occurrence of microbial  
789 sulphur oxidation by long-range electron transport in the seafloor. *ISME J.* **8**: 1843–  
790 1854. doi:10.1038/ismej.2014.41
- 791 Marzocchi, U., D. Trojan, S. Larsen, R. L. Meyer, N. P. Revsbech, A. Schramm, L. P.  
792 Nielsen, and N. Risgaard-Petersen. 2014. Electric coupling between distant nitrate

793 reduction and sulfide oxidation in marine sediment. *ISME J.* **8**: 1682–1690.  
794 doi:10.1038/ismej.2014.19

795 Meysman, F. J. R., N. Risgaard-Petersen, S. Y. Malkin, and L. P. Nielsen. 2015. The  
796 geochemical fingerprint of microbial long-distance electron transport in the seafloor.  
797 *Geochim. Cosmochim. Acta* **152**: 122–142. doi:10.1016/j.gca.2014.12.014

798 Müller, H., J. Bosch, C. Griebler, L. R. Damgaard, L. P. Nielsen, T. Lueders, and R. U.  
799 Meckenstock. 2016. Long-distance electron transfer by cable bacteria in aquifer  
800 sediments. *ISME J.* **10**: 2010–2019. doi:10.1038/ismej.2015.250

801 Nielsen, L. P., and N. Risgaard-Petersen. 2015. Rethinking sediment biogeochemistry after  
802 the discovery of electric currents. *Annu. Rev. Mar. Sci.* **7**: 425–442.  
803 doi:10.1146/annurev-marine-010814-015708

804 Nielsen, L. P., N. Risgaard-Petersen, H. Fossing, P. B. Christensen, and M. Sayama. 2010.  
805 Electric currents couple spatially separated biogeochemical processes in marine  
806 sediment. *Nature* **463**: 1071–1074. doi:10.1038/nature08790

807 Pernthaler, A., J. Pernthaler, and R. Amann. 2002. Fluorescence In Situ Hybridization and  
808 Catalyzed Reporter Deposition for the Identification of Marine Bacteria. *Appl.*  
809 *Environ. Microbiol.* **68**: 3094–3101. doi:10.1128/AEM.68.6.3094-3101.2002

810 Pernthaler, J., F. Glockner, W. Schonhuber, and R. Amann. 2001. Fluorescence in situ  
811 hybridization (FISH) with rRNA-targeted oligonucleotide probes. *Methods Microbiol.*  
812 **30**: 207–226. doi: 10.1016/S0580-9517(01)30046-6

813 Pfeffer, C., S. Larsen, J. Song, and others. 2012. Filamentous bacteria transport electrons over  
814 centimetre distances. *Nature* **491**: 218–221. doi:10.1038/nature11586

815 Rao, A. M. F., S. Y. Malkin, S. Hidalgo-Martinez, and F. J. R. Meysman. 2016. The impact of  
816 electrogenic sulfide oxidation on elemental cycling and solute fluxes in coastal  
817 sediment. *Geochim. Cosmochim. Acta* **172**: 265–286. doi:10.1016/j.gca.2015.09.014

818 Rao, A. M. F., S. Y. Malkin, F. Montserrat, and F. J. R. Meysman. 2014. Alkalinity  
819 production in intertidal sands intensified by lugworm bioirrigation. *Estuar. Coast.*  
820 *Shelf Sci.* **148**: 36–47. doi:10.1016/j.ecss.2014.06.006

821 Risgaard-Petersen, N., M. Kristiansen, R. B. Frederiksen, and others. 2015. Cable Bacteria in  
822 Freshwater Sediments. *Appl. Environ. Microbiol.* **81**: 6003–6011.  
823 doi:10.1128/AEM.01064-15

824 Risgaard-Petersen, N., A. Revil, P. Meister, and L. P. Nielsen. 2012. Sulfur, iron-, and  
825 calcium cycling associated with natural electric currents running through marine  
826 sediment. *Geochim. Cosmochim. Acta* **92**: 1–13. doi:10.1016/j.gca.2012.05.036

827 Sayama, M. 2011. Seasonal dynamics of sulfide oxidation processes in Tokyo Bay dead zone  
828 sediment. **Goldschmidt Conference Abstracts**.

829 Schauer, R., N. Risgaard-Petersen, K. U. Kjeldsen, J. J. Tataru Bjerg, B. B. Jørgensen, A.  
830 Schramm, and L. P. Nielsen. 2014. Succession of cable bacteria and electric currents  
831 in marine sediment. *ISME J.* **8**: 1314–1322. doi:10.1038/ismej.2013.239

832 Seitaj, D., R. Schauer, F. Sulu-Gambari, S. Hidalgo-Martinez, S. Y. Malkin, L. D. W.  
833 Burdorf, C. P. Slomp, and F. J. R. Meysman. 2015. Cable bacteria generate a firewall  
834 against euxinia in seasonally hypoxic basins. *Proc. Natl. Acad. Sci. U. S. A.* **112**:  
835 13278–13283. doi:10.1073/pnas.1510152112

836 Seitaj, D., F. Sulu-Gambari, L. D. W. Burdorf, A. Romero-Ramirez, O. Maire, S. Y. Malkin,  
837 C. P. Slomp, and F. J. R. Meysman. 2017. Sedimentary oxygen dynamics in a  
838 seasonally hypoxic basin. *Limnol. Oceanogr.* **62**: 452–473. doi:10.1002/lno.10434

839 Soetaert, K., and F. Meysman. 2012. Reactive transport in aquatic ecosystems: Rapid model  
840 prototyping in the open source software R. *Environ. Model. Softw.* **32**: 49–60.  
841 doi:10.1016/j.envsoft.2011.08.011

842 Soetaert, K., T. Petzoldt, and F. Meysman. 2010a. Marelac: Tools for aquatic sciences, R  
843 package version.

844 Soetaert, K., T. Petzoldt, and R. Setzer. 2010b. Solving differential equations in R: Package  
845 deSolve. *J. Stat. Softw.* **33**: 1–25.

846 Stoll, M. H. C., K. Bakker, G. H. Nobbe, and R. R. Haese. 2001. Continuous-Flow Analysis  
847 of Dissolved Inorganic Carbon Content in Seawater. *Anal. Chem.* **73**: 4111–4116.  
848 doi:10.1021/ac010303r

849 Stumm, W., and J. J. Morgan. 1981. Aquatic chemistry: an introduction emphasizing  
850 chemical equilibria in natural waters, p. 795–795. *In* Aquatic chemistry: An  
851 introduction emphasizing chemical equilibria in natural waters.

852 Vasquez-Cardenas, D., J. van de Vossenberg, L. Polerecky, and others. 2015. Microbial  
853 carbon metabolism associated with electrogenic sulphur oxidation in coastal  
854 sediments. *ISME J.* **9**: 1966–1978. doi:10.1038/ismej.2015.10

855 van de Velde, S., L. Lesven, L. D. W. Burdorf, S. Hidalgo-Martinez, J. S. Geelhoed, P. Van  
856 Rijswijk, Y. Gao, and F. J. R. Meysman. 2016. The impact of electrogenic sulfur  
857 oxidation on the biogeochemistry of coastal sediments: A field study. *Geochim.*  
858 *Cosmochim. Acta* **194**: 211–232. doi:10.1016/j.gca.2016.08.038

859

860

861 **Figure captions**

862

863 **Figure 1:** The setup of the sediment incubations. Arrows indicate the direction of the water  
864 flow. The sediment cores were incubated in a sediment incubation chamber which was  
865 connected to a water reservoir. An oxygen optode connected to a PC continuously measured  
866 the oxygen concentration within the water reservoir. When the measured oxygen  
867 concentration was 2.5% over or below the wanted concentration, the outlet to either the  
868 N<sub>2</sub>/CO<sub>2</sub> gas (to lower the O<sub>2</sub>) or to the air pump (to raise the O<sub>2</sub>) was opened.

869

870 **Figure 2:** Microsensor depth profiles of the oxygen treatments over time. Sediments of all  
871 treatments were profiled repeatedly over the timespan of the experiment (109 days). For each  
872 time point in every treatment one set of representative microprofiles is depicted. No cable  
873 bacteria activity was recorded in the 10% treatment.

874

875 **Figure 3:** Activity parameters of the cable bacteria derived from the microsensor depth  
876 profiles over time. Each color is one oxygen treatment. (a) Changes in delta pH over time,  
877 where delta pH is the difference in pH between the anodic and cathodic zones of cable  
878 bacteria growth. (b) Changes in suboxic zone width through time, where suboxic zone is  
879 measured as the distance between the oxygen penetration depth and the sulfide appearance  
880 depth. (c) Changes in dissolved oxygen uptake rate (DOU) over time.

881

882 **Figure 4:** Cable bacteria length density in the different treatments at day 39 as quantified  
883 using fluorescent in situ hybridization. Abundances are given in m of cable bacteria per cm<sup>-3</sup>  
884 of sediment. Dotted line indicates the depth at which sulfide is available in the sediment core

885 (or sulfide appearance depth, SAD). Oxygen penetration depth is less than 0.5 cm in all  
886 treatments.

887

888 **Figure 5:** Pore water solute depth profiles at day 39. for (a)  $\text{Fe}^{2+}$ , (b)  $\text{Mn}^{2+}$ , (c)  $\text{Ca}^{2+}$ , (d)  $\text{Mg}^{2+}$ ,  
889 (e) Total Alkalinity (TA) and (f)  $\text{NH}_4^+$ . The line is the mean value of two sediment-cores.  
890 Each color is one oxygen treatment.

891

892 **Figure 6:** Model estimation of the mineralization rate in the sediment cores. A simple reactive  
893 transport model was set up to estimate the carbon and nitrogen mineralization rate in each  
894 treatment. Nitrogen mineralization is here assumed to be the same as ammonification. The  
895 rows are the different oxygen concentration. Points are the measured concentrations and the  
896 lines the modelled TA and  $\text{NH}_4^+$  concentrations.

897

898 **Figure 7:** A schematic representation of the iron and sulfur cycling in a sediment with e-SOx  
899 activity. The sediment is divided into three zones: the oxic, suboxic and anoxic zone. Arrows  
900 between boxes are fluxes which are quantified and given in Table 3. Cable bacteria activity  
901 induces the dissolution of iron-sulfide (box FeS, rate ISD) into  $\text{H}_2\text{S}$  and  $\text{Fe}^{2+}$  in the suboxic  
902 zone. Ferrous iron can then diffuse upwards to the oxic zone, leading to oxidation to FeOOH  
903 (rate FIO) or downwards to the anoxic zone to re-precipitate as FeS (rate ISP). Total sulfide  
904 available for e-SOx equals the sulfate reduction in the suboxic zone (SRR 1), and the upward  
905 flux of sulfide ( $F_{\text{up}}$ ) formed in the anoxic zone (SRR 2) and the sulfide from FeS dissolution  
906 (ISD).

907 **Figure 8:** Schematic representation of the small transparent sediment chamber that was dug  
908 into the sediment to image the sediment-water interface (left). On the right two images which

909 show cable bacteria sticking out of the sediment at lower O<sub>2</sub> concentrations (top) and no cable  
910 bacteria sticking out at higher O<sub>2</sub> concentrations (bottom).

911

912 **Figure 9:** A summary figure of the effect of oxygen availability at day 39 on the dissolved  
913 oxygen uptake (DOU), delta pH and Fe<sup>2+</sup> inventory. Height of the bars indicate the mean,  
914 lines the standard deviation.

915

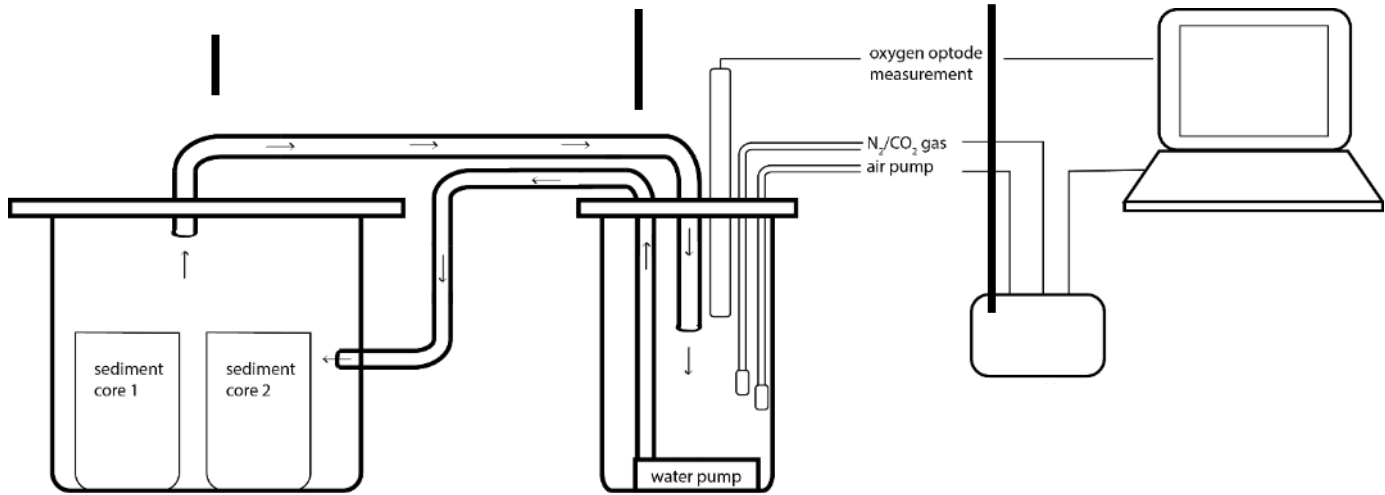


Sediment incubation chamber

Water reservoir

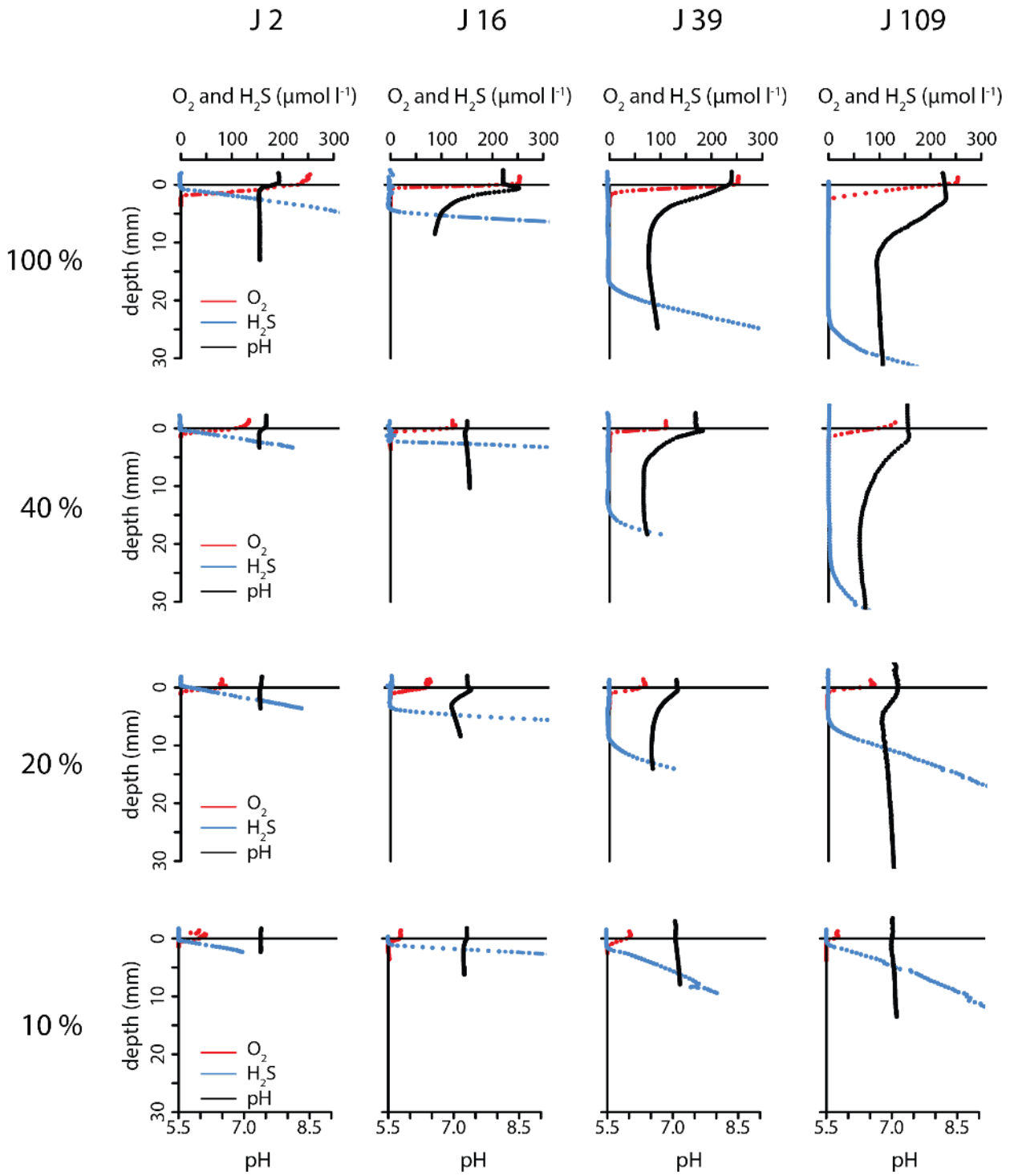
Control box

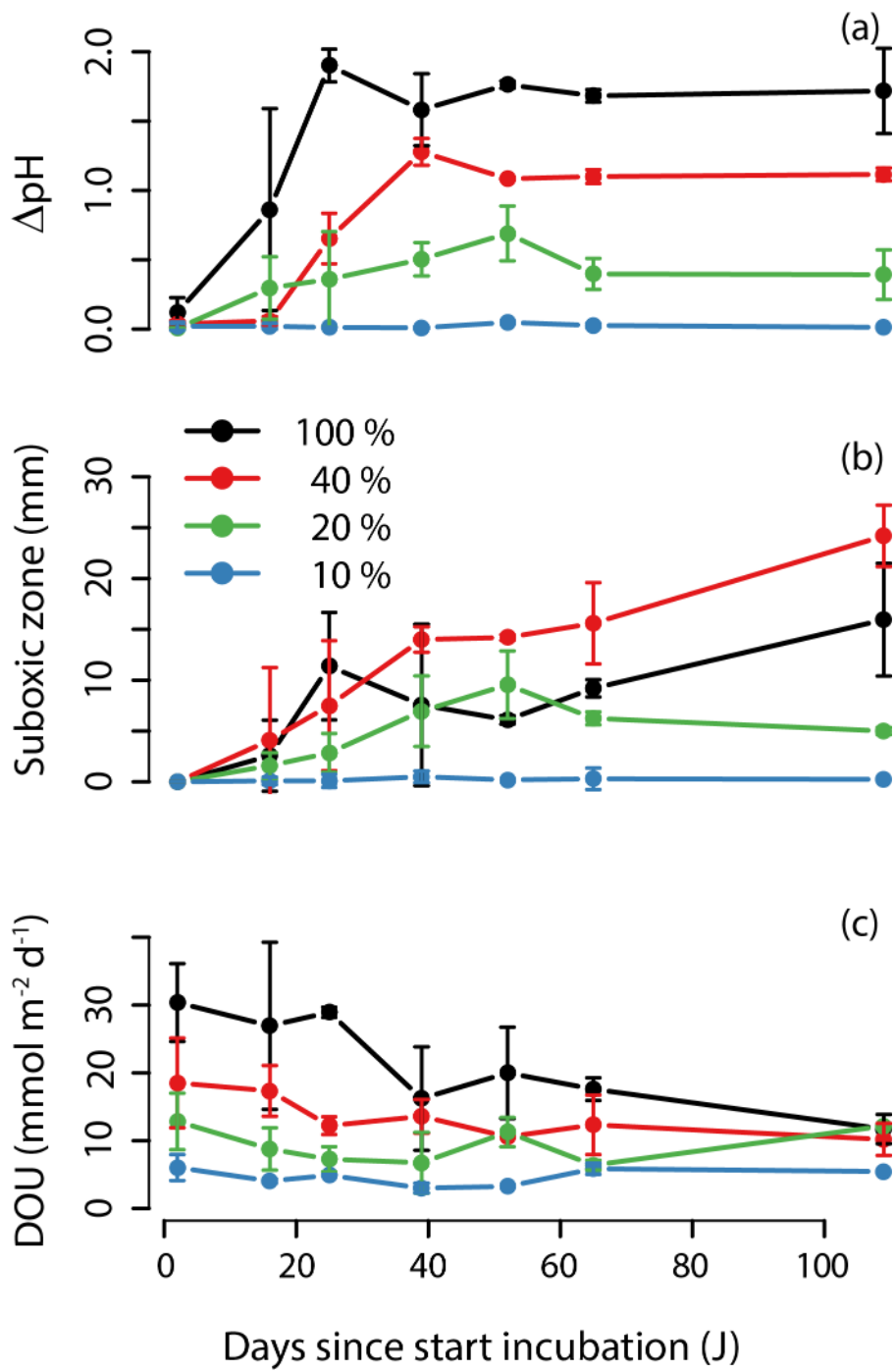
Computer



917 Figure 2

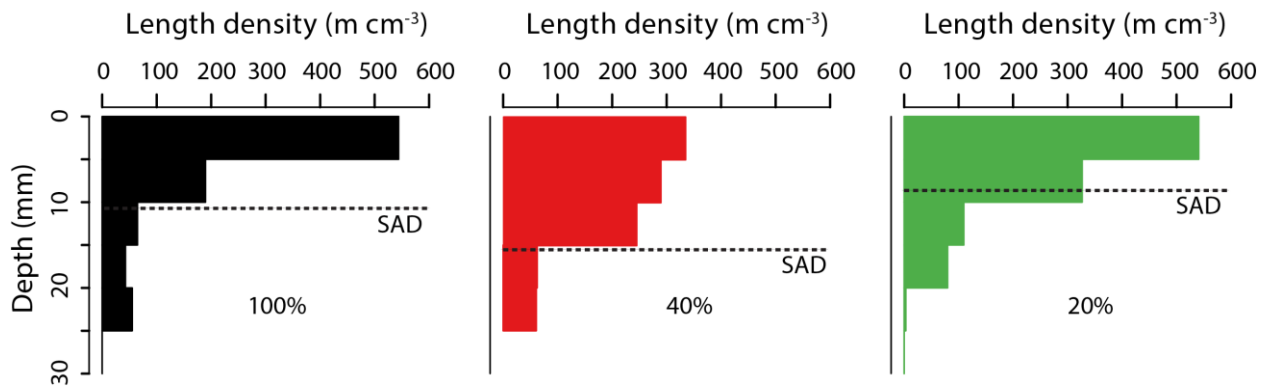
918

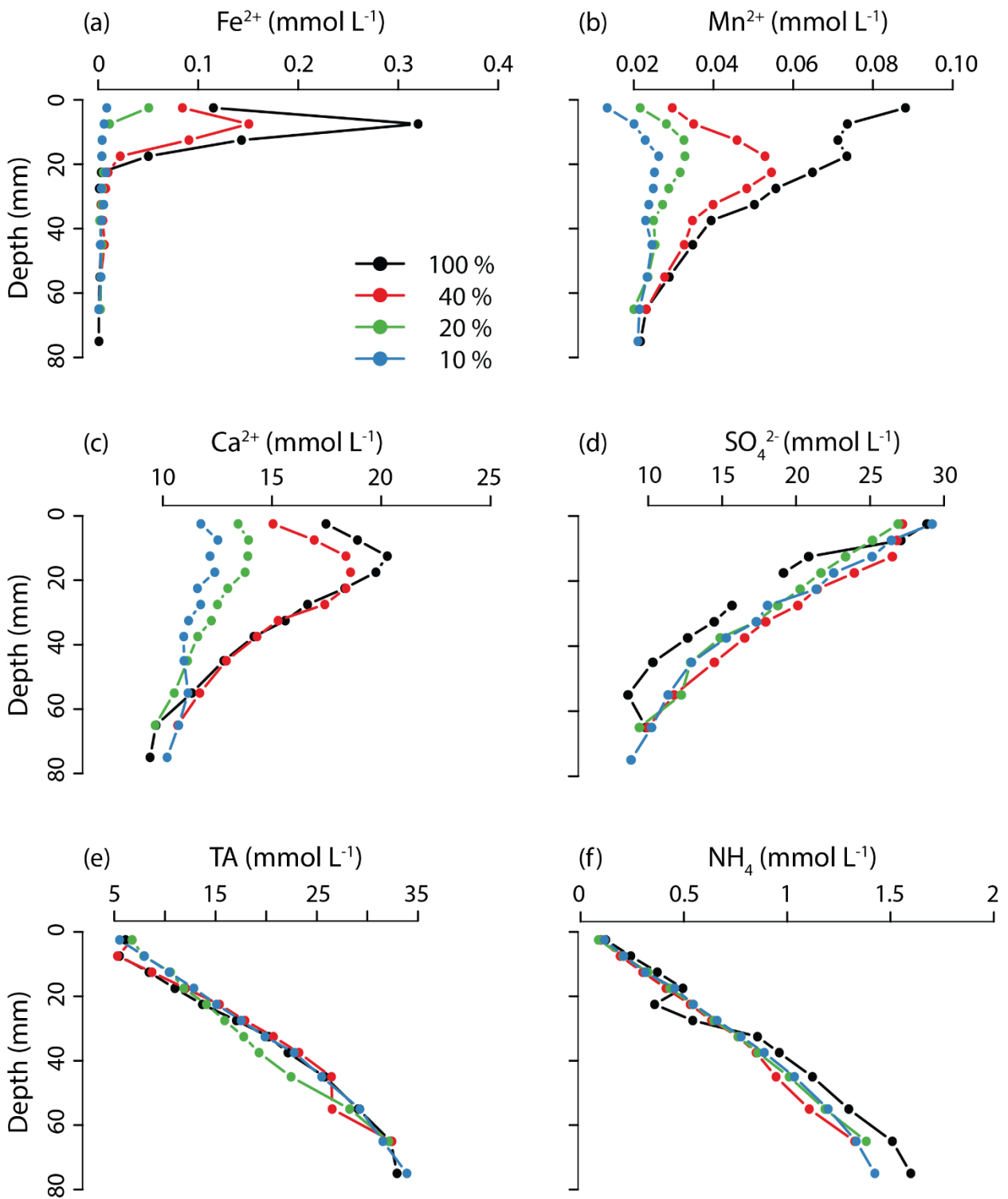




921 Figure 4

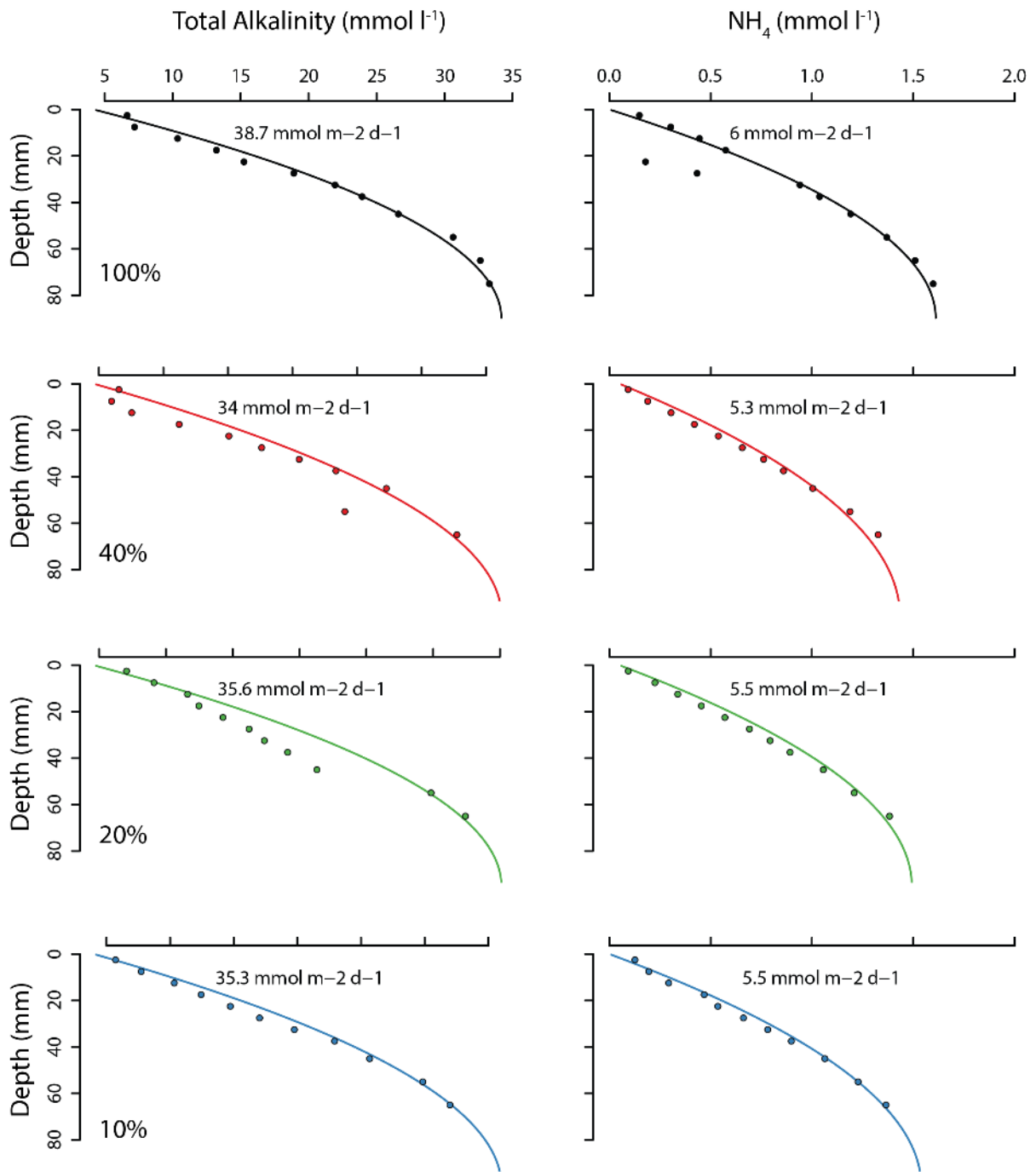
922

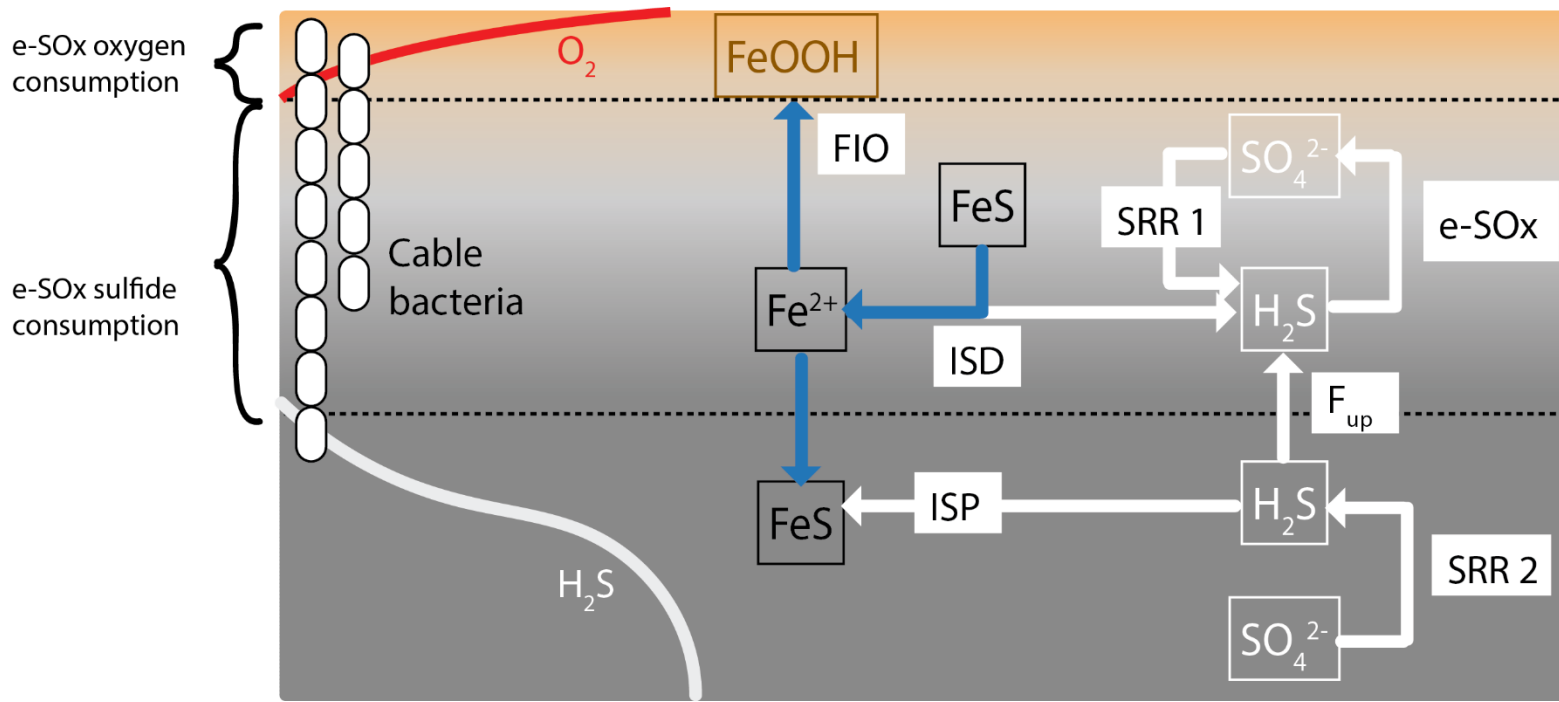




925 Figure 6

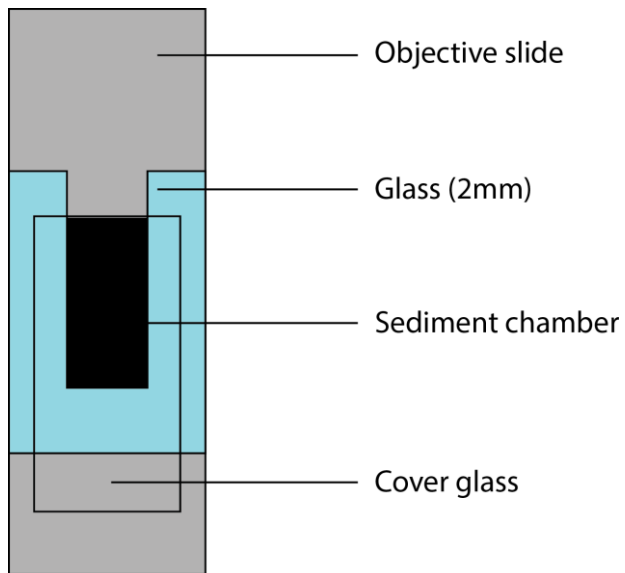
926



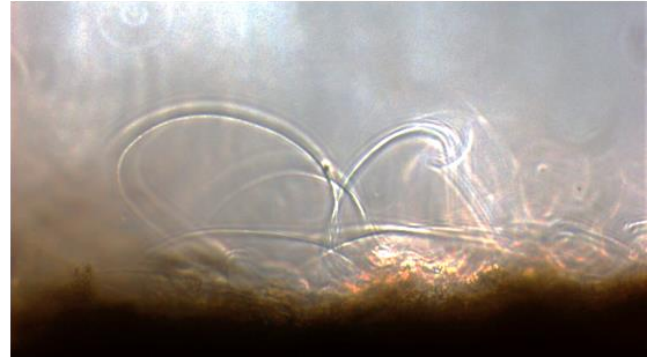


929 Figure 8

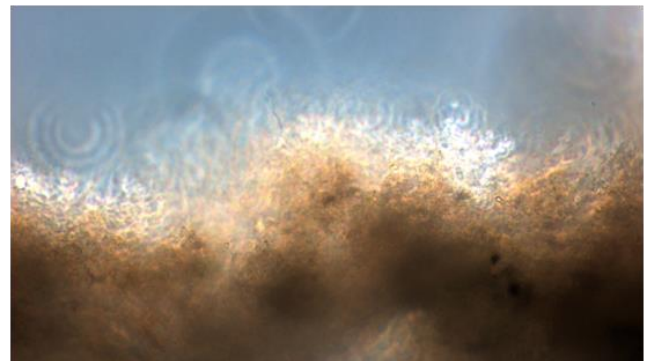
930



$O_2$ :  $160 \mu\text{mol L}^{-1}$



$O_2$ :  $268 \mu\text{mol L}^{-1}$

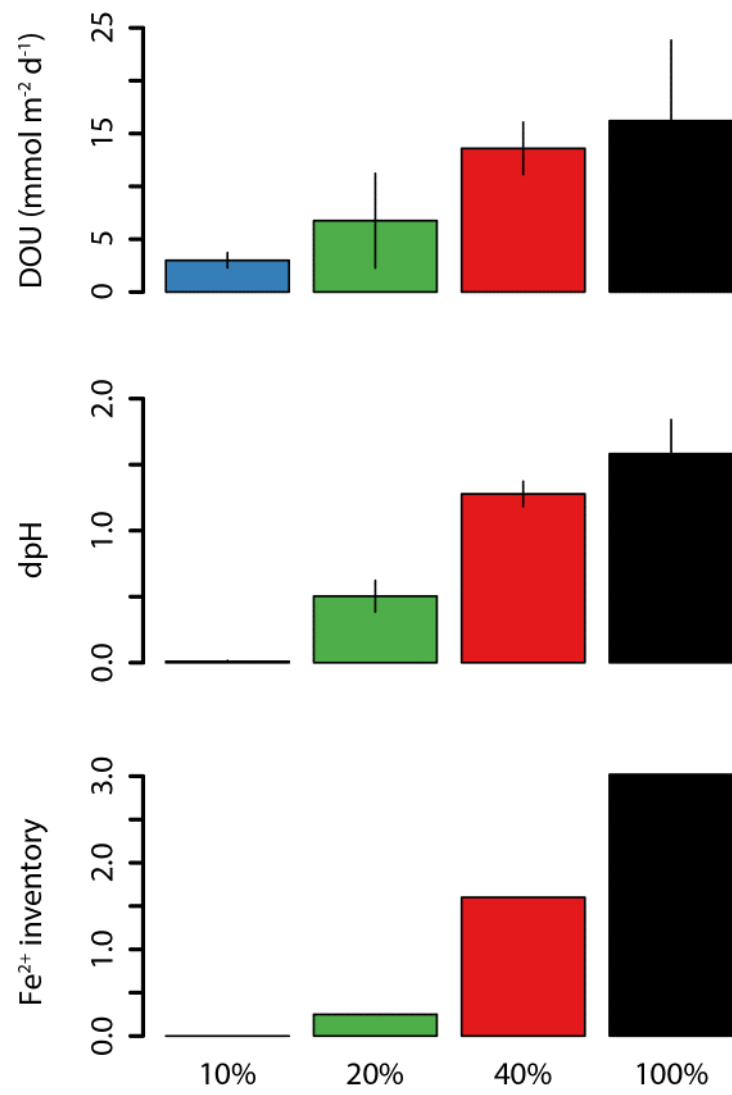


931 Figure 9

932

933

934



935 **Table 1:** Overview of the characteristics of the Lake Grevelingen sediment used in this  
 936 experiment. Values are given as mean  $\pm$  standard deviation.

Lake Grevelingen			Unit	Reference	937
Porosity	0.88	$\pm 0.03$	-	<i>This study</i>	938
Solid phase density	2.6	$\pm 0.03$	g cm <sup>-3</sup>	Rao et al. 2016	939
Median grain size	16.00	$\pm 0.01$	$\mu\text{m}$	<i>This study</i>	
Organic C content	3.4	$\pm 0.2$	% weight	Rao et al. 2016	940
Inorganic C content	2.6	$\pm 0.2$	% weight	Rao et al. 2016	
CaCO <sub>3</sub>	22.0	$\pm 0.4$	% weight	Rao et al. 2016	941
C:N ratio	6.4	-	-	<i>This study</i>	942

943 **Table 2:** Overview of the inventories of dissolved Fe<sup>2+</sup>, Mn<sup>2+</sup>, Ca<sup>2+</sup> in the pore water and  
 944 cable bacteria abundance (filament length density) after 39 days of incubation. Inventories of  
 945 pore water solutes (mmol m<sup>-2</sup>) were calculated as the depth integral of the pore water  
 946 concentration over the top 8 cm and are displayed as the difference in inventory compared to  
 947 the 10% O<sub>2</sub> treatment. Abundance of cable bacteria (in m of cable bacteria per cm<sup>2</sup>) is  
 948 calculated as the depth integral of the filament length density as displayed in Figure 4.

	<b>Unit</b>	<b>10%</b>	<b>20%</b>	<b>40%</b>	<b>100%</b>
Fe <sub>d</sub> inventory	mmol m <sup>-2</sup>	0	0.25	1.60	3.050
Mn <sub>d</sub> inventory	mmol m <sup>-2</sup>	0	0.29	0.99	1.77
Ca <sub>d</sub> inventory	mmol m <sup>-2</sup>	0	59	235	240
Filament length density	m cm <sup>-2</sup>	0	530	502	439

953 **Table 3:** Overview of all fluxes and rates calculated in the various oxygen treatments at  
954 Day39 of the sediment incubations. The corresponding scheme of elemental cycling  
955 schematic is found in Figure 7. [1] The total mineralization rate  $R_{min}$  was obtained from the  
956 model fit to the ammonium and alkalinity profiles. [2] The total sulfate reduction was  
957 estimated as  $SRR = 0.5 * R_{min}$ , thus assuming that sulfate reduction is the primary  
958 mineralization pathway and that other pathways are quantitatively unimportant. [3] The  
959 upward flux of free sulfide from the sulfidic to the suboxic zone ( $F_{up}$ ) was calculated from the  
960 microsensor depth profiles of  $H_2S$ . [4] The rate of FeS dissolution in the suboxic zone (ISD)  
961 was calculated from the  $Fe^{2+}$  depth profiles as the sum of the upward and downward fluxes  
962 away from the subsurface  $Fe^{2+}$  maximum. [5] The rate of FeS re-precipitation (ISP) at the  
963 upper boundary of the sulfidic zone was calculated as the downward  $Fe^{2+}$  flux away from the  
964 subsurface maximum. [6] The rate of ferrous iron oxidation within the oxic zone (FIO) was  
965 calculated as the upward  $Fe^{2+}$  flux away from the subsurface maximum, thus assuming that  
966 no  $Fe^{2+}$  diffuses out of the sediment. [7] The rate of sulfate reduction in the sulfidic zone was  
967 estimated as  $SRR_2 = F_{up} + ISP$  [8] The rate of sulfate reduction in the suboxic zone was  
968 estimated as the difference between the total rate and that in the sulfidic zone  $SRR_1 = SRR -$   
969  $SRR_2$  [9] The rate of electrogenic sulfur oxidation is finally calculated as  $eSO_x = F_{up} + ISD$   
970  $+ SRR_1$ . [10] The dissolved oxygen uptake (DOU) is calculated using Fick's first law from  
971 the microsensor depth profiles.

972

973

974

975

976

977

978

		Unit	10%	20%	40%	100%
C mineralisation	Rmin	mmol C m <sup>-2</sup> d <sup>-1</sup>	35.3	35.6	34.0	38.7
N mineralisation	Nmin	mmol N m <sup>-2</sup> d <sup>-1</sup>	5.5	5.5	5.3	6.5
Sulfate reduction	SRR	mmol S m <sup>-2</sup> d <sup>-1</sup>	17.7	17.8	17.0	19.4
	SRR1	mmol S m <sup>-2</sup> d <sup>-1</sup>	<i>n.d.</i>	2.01	2.86	3.64
	SRR2	mmol S m <sup>-2</sup> d <sup>-1</sup>	<i>n.d.</i>	15.8	14.1	15.8
Upward H <sub>2</sub> S flux	Fup	mmol S m <sup>-2</sup> d <sup>-1</sup>	<i>n.d.</i>	9.2	11.3	12.4
FeS dissolution	ISD	mmol Fe m <sup>-2</sup> d <sup>-1</sup>	<i>n.d.</i>	<i>n.d.</i>	0.94	2.47
FeS precipitation	ISP	mmol Fe m <sup>-2</sup> d <sup>-1</sup>	<i>n.d.</i>	<i>n.d.</i>	0.46	0.98
Ferrous Iron	FIO	mmol Fe m <sup>-2</sup> d <sup>-1</sup>	<i>n.d.</i>	<i>n.d.</i>	0.48	1.49
Oxidation						
Electrogenic sulfur oxidation	eSOx	mmol S m <sup>-2</sup> d <sup>-1</sup>	<i>n.d.</i>	11.2	15.1	18.5
Diffusive Oxygen Uptake	DOU	mmol O <sub>2</sub> m <sup>-2</sup> d <sup>-1</sup>	3.5 ± 0.8	6.8 ± 5.1	13.6 ± 2.5	16.2 ± 7.6

979

980